Spatial and Temporal Patterns in Petrogenic Organic Carbon Mobilisation during the Paleocene-Eocene Thermal Maximum

E. H. Hollingsworth[1*], F. J. Elling[2,3], M. P. S. Badger[4], R. D. Pancost[5], A. J. Dickson[4,6], R. L. Rees-Owen[5], N. M. Papadomanolaki[7,8], A. Pearson[2], A. Sluijs[7], K. H. Freeman[9], A. A. Baczynski[9], G. L. Foster[1], J. H. Whiteside[1,10], and G. N. Inglis[1*]

[1] School of Ocean and Earth Science, University of Southampton, Southampton, UK

[2] Department of Earth and Planetary Sciences, Harvard University, Cambridge, MA, USA

[3] Leibniz-Laboratory for Radiometric Dating and Isotope Research, Christian-Albrechts, University of Kiel, Kiel, Germany

[4] School of Environment, Earth and Ecosystem Sciences, The Open University, Milton Keynes, UK

[5] Department of Earth Sciences and School of Chemistry, University of Bristol, Bristol, UK

[6] Centre of Climate, Ocean and Atmosphere, Department of Earth Sciences, Royal Holloway University of London, Surrey, UK

[7] Department of Earth Sciences, Utrecht University, Utrecht, Netherlands

[8] Now at Institue für Geologie and Paläontologie, Universität Münster, Münster, Germany

[9] Department of Geosciences, The Pennsylvania State University, State College, PA, USA

[10] Now at Department of Earth and Environmental Sciences, San Diego State University, San Diego, CA, USA

*Corresponding author: Gordon N. Inglis (Gordon.inglis@soton.ac.uk) and Emily H. Hollingsworth (e.hollingsworth@soton.ac.uk)

Key Points:

- We assess spatial and temporal patterns in petrogenic organic carbon (OC_{petro}) mobilisation during the PETM
- Enhanced OC_{petro} mobilisation in the subtropics and mid-latitudes, likely due to an increase in extreme rainfall events
- Mobilisation of OC_{petro} remained elevated during the recovery phase of the PETM

Abstract

The Paleocene-Eocene Thermal Maximum (PETM) was a transient global warming event recognised in the geologic record by a prolonged negative carbon isotope excursion (CIE). The onset of the CIE was the result of a rapid influx of ^{13}C-depleted carbon into the ocean-atmosphere system. However, the mechanisms required to sustain the negative CIE remains unclear. Previous studies have identified enhanced mobilisation of petrogenic organic carbon (OC_{petro}) and argued that this was likely oxidised, increasing atmospheric carbon dioxide (CO_2) concentrations after the onset of the CIE. With existing evidence limited to the mid-latitudes and subtropics, we determine whether: (i) enhanced mobilisation and subsequent burial of OC_{petro} in marine sediments was a global phenomenon; and (ii) whether it occurred throughout the PETM. To achieve this, we utilised a lipid biomarker approach to trace and quantify OC_{petro} burial in a global compilation of PETM-aged shallow marine sites (n = 7, including five new sites). Our results confirm that OC_{petro} mass accumulation rates (MARs) increased within the subtropics and mid-latitudes during the PETM, consistent with evidence of higher physical erosion rates and intense episodic rainfall events. The high-latitude sites do not exhibit distinct changes in the organic carbon source during the PETM. This may be due to the more stable hydrological regime and/or additional controls. Crucially, we also demonstrate that OC_{petro} MARs remained elevated during the recovery phase of the PETM. Although OC_{petro} oxidation was likely an important positive feedback mechanism throughout the PETM, we show that this feedback was both spatially and temporally variable.

Plain Language Summary

The Paleocene-Eocene Thermal Maximum (PETM) was the most severe global warming event of the last 66 million years, caused by natural and rapid release of greenhouse gases into the atmosphere. However, scientists have been unable to determine why the PETM lasted for > 100,000 years. Several theories suggest further emission of greenhouse gases from positive feedback mechanisms triggered by early onset warming. Here, we explore one such mechanism: CO_2 released from the erosion, transport, and oxidation of ancient rock-derived (or petrogenic) organic carbon, and identify if it occurred globally and/or throughout the PETM. We achieve this by looking at biomarkers (molecular fossils) and use this approach to trace the input of

petrogenic organic carbon into the marine realm. Results suggest enhanced transport of petrogenic organic carbon was restricted to the subtropics and mid-latitudes, with limited changes in the high-latitudes. We also find evidence for erosion and transport of petrogenic organic carbon throughout the PETM. Therefore, this process likely contributed to increasing atmospheric CO_2 levels and may have been an important positive feedback mechanism in past and future warm climates.

1 Introduction

Climate and tectonics have modulated the flux of carbon to and from terrestrial reservoirs over geological timescales. Early studies predominantly focused on understanding the role of inorganic carbon, for example, carbon dioxide (CO_2) released from solid Earth degassing versus CO_2 drawdown from silicate weathering (e.g., Berner et al., 1983; Caldeira & Berner, 1997; Walker et al., 1981). However, the past two decades have highlighted the importance of the terrestrial organic carbon cycle as a climate feedback mechanism (Hilton & West, 2020). Whether it acts as a positive or negative feedback mechanism largely depends on whether the organic carbon is 'biospheric' (OC_{bio}), representing relatively recent thermally immature organic carbon (10^2–10^4 years old; e.g., vegetation and soils), or 'petrogenic' (OC_{petro}), representing ancient rock-derived and thermally mature organic carbon (> 10^6 years old; e.g., organic carbon-rich shales). Erosion, mobilisation, and the subsequent burial of OC_{bio} in marine sediments sequesters CO_2 (Berhe et al., 2007; Stallard, 1998). In contrast, exhumation and oxidation of OC_{petro} during lateral transport from land-to-sea can release CO_2 (Petsch et al., 2000). Observations on modern fluvial systems suggest that the fraction of OC_{petro} oxidised positively correlates with the transit duration (Hilton & West, 2020). Up to ~90 % of OC_{petro} is oxidised in large catchments, such as the Amazon and Himalayan range (e.g., Bouchez et al., 2010; Galy et al., 2008), whereas a lower proportion (~10–40 %) of OC_{petro} is oxidised in mountain basins with steep rivers (e.g., Hilton et al., 2011, 2014). Thus, regardless of catchment dynamics, OC_{petro} has the potential to be oxidised and increase atmospheric CO_2 concentrations.

Several studies have quantified the mobilisation and burial of OC_{petro} in modern systems (e.g., Blair et al., 2003; Clark et al., 2017, 2022; T. I. Eglinton et al., 2021 and references therein; Galy et al., 2007, 2015 and references therein; Hilton et al., 2010, 2011; Hilton & West, 2020 and

references therein; Smith et al., 2013) and Holocene sediments (e.g., Hilton et al., 2015; Kao et al., 2008, 2014). While there is a bias towards environments where erosion and transport of terrestrial organic carbon is largely controlled by geomorphic processes, climate is also seen as a strong regulator (e.g., T. I. Eglinton et al., 2021; Hilton, 2017). For example, extreme rainfall events can trigger bedrock landslides (e.g., Hilton et al., 2008) and/or create deeply incised gullies (e.g., Leithold et al., 2006), both of which can increase the quantity of OC_{petro} transferred and exposed to atmospheric oxidation. Although, the resulting high abundance of clastic sediments from hyperpycnal flows and turbidites may also enhance the preservation of OC_{petro} (e.g., Bouchez et al., 2014; Hilton et al., 2011). As climate model simulations indicate an intensification of the hydrological cycle in response to rising atmospheric CO_2 levels and global temperatures (Lee et al., 2021), the delivery of OC_{petro} to the oceans will likely be enhanced in the future. However, such predictions are based on present-day observations and/or past climate states that span a lower-than-modern atmospheric CO_2 values.

In contrast, the geological record enables investigations into high CO_2 states of the past, providing unique insights on how terrestrial carbon cycle processes may operate in the future. Many studies have focused on the Paleocene-Eocene Thermal Maximum (PETM; ~56 million years ago) (McInerney & Wing, 2011), a transient global warming event (e.g., mean surface temperature increase of ~4–6 ºC; Inglis et al., 2020; Tierney et al., 2022) associated with an intensified hydrological cycle (Carmichael et al., 2017 and references therein). The PETM is identified in the geologic record by a negative carbon isotope excursion (CIE) (e.g., -4 ± 0.4 ‰; Elling et al., 2019). The onset of the PETM is on the order-of-millennia (Kirtland Turner, 2018; Zeebe et al., 2014) and is followed by sustained low and stable carbon isotope ($\delta^{13}C$) values for ~94–170 thousand years (kyrs) (Zeebe & Lourens, 2019), referred to as the "body" of the CIE (Bowen et al., 2006). The body is then followed by a long recovery of ~50–120 kyrs (Bowen, 2013; Murphy et al., 2010; Zeebe et al., 2009), which is further divided into Phase I (initial rapid rise in $\delta^{13}C$) and Phase II (final gradual rise in $\delta^{13}C$) (Röhl et al., 2007).

The onset of the CIE was the result of a rapid influx of ^{13}C-depleted carbon from one or more reservoirs outside the active global exogenic carbon pool (Dickens et al., 1997). Proposed

reservoirs include submarine methane hydrates (Dickens, 2011; Dickens et al., 1995), terrestrial organic carbon (Bowen, 2013; Deconto et al., 2012; Kurtz et al., 2003), and volcanic carbon related to the North Atlantic Igneous Province (Gutjahr et al., 2017; Jones et al., 2019; Storey et al., 2007; Svensen et al., 2004). Less explored are the mechanism responsible for the prolonged body of the CIE. This feature requires continual input of ^{13}C-depleted carbon (e.g., Zeebe et al., 2009) and several feedback mechanisms (either acting individually or in combination) have been proposed. This includes a slow dissociation of oceanic methane hydrates (Zeebe, 2013) and/or pulsed releases of thermogenic methane from vent complexes (e.g., Frieling et al., 2016; Kirtland Turner, 2018). Alternatively, recent work suggests that CO_2 released from OC_{petro} oxidation could explain the extended body of the CIE (Lyons et al., 2019). This theory is based on evidence for an order-of-magnitude increase in the delivery of OC_{petro} to the oceans, ~10–20 kyrs after the onset of the PETM. However, this study was limited to the mid-latitudes (Atlantic Coastal Plain) and subtropics (Tanzania), and thus may not be globally representative. It is also unclear whether enhanced mobilisation of OC_{petro} was a persistent feature throughout the PETM or whether it was restricted to the body interval.

Here we use lipid biomarker thermal maturity ratios to fingerprint OC_{petro} burial in a global compilation of PETM-aged shallow marine sites (n = 7, including five new sites). Lipid biomarkers undergo various structural alterations with increasing thermal maturity (e.g., defunctionalisation, isomerisation, catagenesis, and aromatisation; Peters et al., 2005) and thus can be used to assess the proportion of OC_{petro} in marine sediments (Lyons et al., 2019). We focus on thermally immature, shallow marine sediments as they are 'hotspots' for terrestrial organic carbon input (Bianchi et al., 2018). We quantify OC_{petro} burial fluxes before and during the PETM, using a two-endmember mixing model. Overall, we aim to determine whether: (i) enhanced mobilisation and subsequent burial of OC_{petro} in the ocean was a global phenomenon; and (ii) whether it occurred throughout the PETM.

2 Methods

2.1 Data compilation

New *n*-alkane- and/or hopane-based thermal maturity ratios were acquired from the following PETM-aged shallow marine sites: the International Ocean Drilling Program Expedition 302 Site

M0004A (or the Arctic Coring Expedition; **ACEX**); the Ocean Drilling Program Site 1172 Hole D (**ODP Site 1172**); **Kheu River**; ODP Leg 174AX Ancora Site Hole A/B (**Ancora**); and the Tanzania Drilling Project Site 14 Hole A (**TDP Site 14**) (Figure 1 and Table S1 in the supporting information). We also compile *n*-alkane- and/or hopane-based thermal maturity ratios from the following published PETM-aged shallow marine sites: TDP Site 14 (Carmichael et al., 2017; Handley et al., 2012); South Dover Bridge (**SDB**) (Lyons et al., 2019); and Cambridge-Dorchester Airport (**CamDor**) (Lyons et al., 2019).

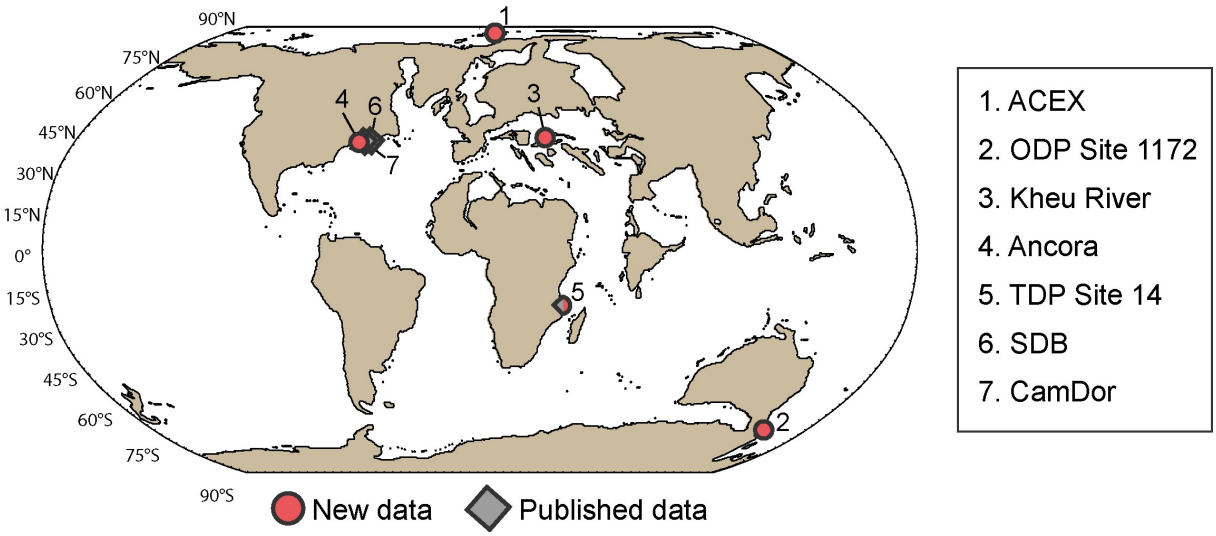

Figure 1: Location of sites with new data (1-5) and published data (5-7). Paleogeographic reconstructions of 56 million years ago, adapted from Carmichael et al., (2017)

2.2 Organic geochemistry

Samples from ACEX (n = 94), ODP Site 1172 (n = 41), and Ancora (n = 42) were freeze dried, homogenized, and extracted using a MARS5 microwave-assisted extraction system, using: (i) dichloromethane:methanol (DCM:MeOH; 1:1, *v*:*v*); (ii) DCM:MeOH (9:1, *v*:*v*); and (iii) DCM (see Elling et al., 2019). Each solvent mixture was heated for 30 minutes to 100 °C, followed by a hold time of 20 minutes. The extracts from the three steps were combined into a total lipid extract (TLE) and further divided into five fractions (following Polik et al., 2018). When required, extracted copper was added to the apolar fractions for 24 hours to remove elemental sulphur. The apolar fractions were analysed using a ThermoFisher Trace 1310 GC coupled to a

Thermo TSQ8000 Triple Quadrupole MS (GC-MS). Helium was used as the carrier gas and separation was achieved with DB-5 column (30 m x 0.25 mm i.d., 0.25 μm film thickness). The GC oven program started at 70 °C for 1 minute, increased to 130 °C at 20 °C min^{-1}, followed by 300 °C at 4 °C min^{-1}, which was then held for 20 minutes. MS scanning occurred between mass-to-charge ratio (*m/z*) 50 to 650 Daltons, and an ionisation energy of 70 eV. Compound identification was based on: retention times; fragmentation patterns; comparison to an in-house standard; and library matches.

Kheu River samples (n = 39) were extracted at the University of Bristol by ultrasonicating homogenised samples sequentially with DCM, DCM:MeOH (1:1, *v*:*v*), and MeOH. Elemental sulphur was removed from the combined TLE using activated copper turnings. An activated silica column with saturated ammonia in chloroform and chloroform:acetic acid (100:1, *v*:*v*) was used to separate the neutral and acid fraction, respectively. The apolar fraction was split from the neutral fraction by eluting with hexane:DCM (9:1, *v*:*v*) via separation on an alumina column. The apolar fractions were then analysed at the University of Bristol on a Thermoquest Finnigan Trace GC interfaced with a Thermoquest Finnigan Trace MS. The GC was fitted with a fused capillary column (50 m x 0.32 mm i.d.) and the carrier gas was helium. The samples were suspended in ethyl acetate and injected at 70 °C. The temperature program increased to 130 °C (20 °C min^{-1}), then 300 °C (4 °C min^{-1}), and finally remained isothermal for 20 minutes. The MS operated with an electron ionisation source at 70 eV, scanning over *m/z* ranges of 50 to 850 Daltons. The compounds were quantified on the total ion chromatogram (TIC).

Additional samples (n = 12) from TDP Site 14 were homogenised and extracted at the University of Bristol. Extractions were achieved via Soxhlet apparatus overnight, using DCM:MeOH (2:1 *v:v*). The apolar fraction was suspended in hexane:DCM (9:1, *v:v*) and separated by alumina column chromatography. Co-eluting compounds and/or unresolved complex mixtures were reduced with urea adduction (following Pancost et al., 2008). Elemental sulphur was removed using extracted copper turnings. The apolar fractions were analysed at the University of Bristol on the same GC-MS as used for Kheu River. The GC was fitted with a CPsil-5CB column (Agilent Technologies, dimethylpolysiloxane stationary phase) and the carrier gas was helium.

The samples were injected in ethyl acetate at 70 °C. The temperature program increased to 130 °C (20 °C min^{-1}), then 300 °C (4 °C min^{-1}), and finally held for 25 minutes. The MS operated with an electron ionisation source at 70 eV, scanning over *m/z* ranges of 50 to 850 Daltons.

2.3 Lipid biomarker proxies

2.3.1 *n*-alkane-based thermal maturity ratios

Modern plants and sediments contain long-chain *n*-alkanes with an odd-over-even preference (G. Eglinton & Hamilton, 1967), however this is progressively lost during diagenesis. The shift away from a dominance of long-chain *n*-alkanes with an odd-over-even predominance is captured by the carbon preference index (CPI) (Bush & McInerney, 2013). Modern sediments exhibit high CPI values (> 3–30), indicating relatively unaltered thermally immature organic matter (Diefendorf & Freimuth, 2017). In contrast, mature organic matter (e.g,. coal, oil) exhibits low CPI values (~1). CPI values < 1 are less common, and typify low-maturity source rocks from carbonates or hypersaline environments. In this study, sites with extensive post-depositional diagenesis were excluded, such that CPI values closer to 1 likely suggests input of allochthonous thermally mature organic matter (e.g., OC_{petro}). Here, we use the equation as originally defined by Bray & Evans (1961):

$$\mathrm{CPI} = \frac{1}{2}\left[\left(\frac{\sum_{\mathrm{odd}}(C_{25-31})}{\sum_{\mathrm{even}}(C_{26-32})}\right) + \left(\frac{\sum_{\mathrm{odd}}(C_{27-33})}{\sum_{\mathrm{even}}(C_{26-32})}\right)\right] \qquad \text{(Eq. 1)}$$

2.3.2 Hopane-based thermal maturity ratios

Hopanes are the diagenetic products of biohopanoids, which are produced by a wide diversity of bacteria and consequently ubiquitous in a range of environments (Kusch & Rush, 2022). The ratios between different hopanes and their various stereoisomers have long been utilised as a thermal maturity proxy in the field of petroleum geochemistry (e.g., Farrimond et al., 1998; Mackenzie et al., 1980). Most of the hopane-based thermal maturity ratios used in this study are normalised (with the exception of Equation 4). Values indicating high thermal maturity likely suggests allochthonous older material (e.g., pre-PETM-aged OC_{petro}), as sites with post-depositional diagenesis were excluded from this study. We use a multi-ratio approach as each ratio corresponds to different stages of maturity relative to the oil window (i.e., from early diagenesis to the generation of oil), thus enabling insight on the degree of thermal maturation

(Figure S1 in the supporting information). However, hopane distributions also vary depending on the lithofacies and/or depositional environment (Peters et al., 2005). Therefore without knowledge of the source rock at each locality, comparison between the sites should be undertaken with caution.

With the exception of *Frankia* spp. (Rosa-Putra et al., 2001), all bacteria synthesise hopanoids with a 17β21β configuration. However, this changes to a more stable βα and then αβ configuration during early diagenesis and then peak oil generation, respectively (Farrimond et al., 1998; Mackenzie et al., 1980). The shift from ββ to αβ is expressed via the following equation (sometimes referred in literature as 'hopanoid isomerisation'):

$$\alpha\beta/(\alpha\beta + \beta\beta) \qquad \text{(Eq. 2)}$$

Higher thermal maturity is marked by values closer to 1. However, caution should be taken when interpreting sediments with input from peats, as C_{31} αβ isomers dominate the hopane distribution within acidic wetland environments (Inglis et al., 2018).

The shift from βα (also referred to as moretane; M) to the more stable αβ (also referred to as hopane; H) is assessed via the following equation (sometimes referred in literature as 'moretane/hopane ratio'):

$$\beta\alpha/(\beta\alpha + \alpha\beta) \qquad \text{(Eq. 3)}$$

This equation is mostly applied using C_{30} hopane (e.g., French et al., 2012), although C_{29} hopane has also been used (Peters et al., 2005). Values closer to ~0 indicate higher thermal maturity and oil generation.

The C_{29} αβ hopane (also referred to as norhopane; N) is more thermally stable than C_{30} αβ hopane. This is assessed via the following equation (sometimes referred in literature as 'norhopane/hopane ratio'):

$C_{29}\ \alpha\beta/C_{30}\ \alpha\beta$ (Eq. 4)

As well as a thermal maturity proxy, this ratio has been utilised to differentiate between anoxic carbonate and/or marl source rocks (> 1) vs. clay-rich source rocks (< 1) (Peters et al., 2005).

Towards the early stages of oil generation, there is a change in stereochemistry at the C-22 position, from the biologically favoured R configuration to a near equal mix of R and S (Farrimond et al., 1998; Mackenzie et al., 1980; Peters et al., 2005). This is expressed via the following equation (sometimes referred in literature as 'homohopane isomerisation'):

$S/(S + R)$ (Eq. 5)

This equation uses $C_{31\text{-}35}$ hopanes (also referred to as homohopanes) and approaches maximum (equilibrium) values of ~0.6 as thermal maturity increases and oil is generated.

At the late stage of oil generation, C_{27} hopanes shift in the position of a D-ring methyl group, from C-18 (17α(H),22,29,30-trisnorhopane; T_m) to C-17 (18α(H),22,29,30-trisnorneohopane; T_s) (Farrimond et al., 1998; Peters et al., 2005). This is expressed via the following equation:

$T_s/(T_s + T_m)$ (Eq. 6)

T_m refers to maturable (less stable), whereas T_s denotes stable. Values closer to 1 indicate higher thermal maturity, although the oxicity of the depositional environment also has a notable influence (Peters et al., 2005).

2.4 Two-endmember mixing models

The fraction of OC_{petro} (f_{petro}) was calculated for each hopane-based thermal maturity ratio (X_{mix}; Table 1), following the two-endmember mixing model from Lyons et al. (2019):

$$X_{\mathrm{mix}} = f_{\mathrm{petro}} \times X_{\mathrm{petro}} + \left(1 - f_{\mathrm{petro}}\right) \times X_{\mathrm{background}} \quad \text{(Eq. 7)}$$

where $X_{background}$ and X_{petro} is the defined immature and mature endmembers, respectively. The endmembers for $C_{31\text{-}35}$ S/(S+R) ratio follow the definitions in Lyons et al. (2019), where $X_{background}$ is the contemporaneous carbon value of 0 and X_{petro} is the most thermally mature value

of 0.6. The endmembers for $C_{29\text{-}30}$ βα/(βα + αβ) ratio also follow the definitions in Lyons et al. (2019), where $X_{background}$ is 1 and X_{petro} is 0. For this study, the endmembers of the αβ/(αβ + ββ) ratio was defined as 0 for $X_{background}$ is 1 for X_{petro}. Note that C_{29} αβ/C_{30} αβ and $T_s/(T_s + T_m)$ ratios were excluded due to their strong dependence on the source rock and/or depositional environment (Peters et al., 2005).

Table 1: The hopane-based thermal maturity ratio (X_{mix}) used to calculate f_{petro}, with assumed linear sedimentation rate (LSR) and total organic carbon (TOC) reference for each site

Site	X_{mix}	**LSR (cm kyr^{-1})**				**TOC references**
		Pre-PETM	**Core PETM**	**Recovery PETM**		
				Phase I	**Phase II**	
ACEX[a]	$C_{30\text{-}31}$ αβ/(αβ + ββ) C_{31} S/(S + R) C_{30} βα/(βα + αβ)	1	Min: 3.8 Max: 6.2			Elling et al. (2019)
ODP Site 1172[b]	$C_{30\text{-}31}$ αβ/(αβ + ββ) C_{31} S/(S + R) C_{30} βα/(βα + αβ)	0.57	Min: 0.4 Max: 0.5	Not available		Papadomanol-aki et al. (2022)
Kheu River[c]	$C_{29\text{-}31}$ αβ/(αβ + ββ) $C_{29\text{-}30}$ βα/(βα + αβ)	0.3	1.9			Dickson et al. (2014)
Ancora[d]	$C_{30\text{-}31}$ αβ/(αβ + ββ) C_{31} S/(S + R) C_{30} βα/(βα + αβ)	0.8	11.2 and 4.3	1.3	8.4	Elling et al. (2019)
TDP Site 14[e]	$C_{29\text{-}31}$ αβ/(αβ + ββ) $C_{31\text{-}35}$ S/(S + R) $C_{29\text{-}30}$ βα/(βα + αβ)	Min: 0.5 Max: 2	Min: 3.5 Max: 14	NA		Aze et al. (2014)
SDB[f]	C_{31} S/(S + R) C_{29} βα/(βα + αβ)*	Min: 1.03 Max: 2.4	14	21.3	21.3	Lyons et al. (2019)
CamDor[f]	C_{29} βα/(βα + αβ)* $C_{31\text{-}32}$ S/(S + R)*	Min: 1.03 Max: 2.4	14			Lyons et al. (2019)

[a-f]References for LSR. [a]Sluijs, Röhl, et al. (2008). [b]Sluijs et al. (2011). [c]John et al. (2008). [d]Stassen et al. (2012). [e]Lyons et al. (2019). [f]Doubrawa et al. (2022).

*f_{petro} calculated in Lyons et al. (2019)

2.5 Mass accumulation rates

The mass accumulation rate (MAR; in gC cm^2 kyr^{-1}) of OC_{petro} was recalculated for all the new and published f_{petro} data, following Lyons et al. (2019):

$$\mathrm{MAR} = \mathrm{LSR} \times \rho \times f_{\mathrm{petro}} \times \frac{\mathrm{TOC}}{100} \qquad \text{(Eq. 8)}$$

, where LSR is the linear sedimentation rate (cm kyr^{-1}), ρ is the dry bulk density (g cm^{-3}), and TOC is the total organic carbon (%). A constant ρ value of 1.8g cm^{-3} was assumed across all the sites. The TOC values and LSR were acquired for each location from previously published studies (Table 1). TOC records from ODP Site 1172 (Papadomanolaki et al., 2022) and TDP Site 14 (Aze et al., 2014) were linearly interpolated to match the depths of the biomarker data, using R Package Astrochron (Meyers, 2014). LSR estimates were obtained (where possible) for three key time intervals: (i) pre-PETM (Paleocene); (ii) the "core" (onset and body of the CIE) of the PETM; (iii) and the recovery of the PETM (see Text S1 in the supporting information). This was available for all the sites with the exception ODP Site 1172, which lacks the recovery interval. Note that the recovery at Ancora and SDB was further divided into: (iiia) Phase I; and (iiib) Phase II. Since Kheu River does not have LSR data, estimates were taken from the nearby Aktumsuk section (Uzbekistan; John et al., 2008). Both sites comprise shallow marine deposits that exhibits TOC values from ~0 % pre-PETM to a maximum of ~8.5 % during the PETM (Bolle et al., 2000; Dickson et al., 2014). Similarly, LSRs from within the core interval of SDB was assumed to be the same for the entire PETM section at CamDor (following Lyons et al., 2019).

3 Results

3.1 Thermal maturity ratios

3.1.1 ACEX

The apolar fraction contains short- (C_{15-19}), mid- (C_{21-25}), and long- (C_{27-33}) chain *n*-alkanes, and C_{27} to C_{32} hopanes (including αβ, βα, and ββ isomers). Both CPI (ranging from ~1–3) and hopane-based thermal maturity ratios exhibit relatively stable trends throughout the sequence, suggesting that the organic carbon source did not distinctly change (Figure 2). Note that potential information may be missing due poor core recovery between ~388–384.5 mcd (Sluijs et al., 2006). However, C_{30} αβ/(αβ + ββ), C_{31} S/(S + R), and $T_s/(T_s + T_m)$ values slightly increase (i.e., higher thermal maturity) between pre-PETM and the core of the PETM, by an average of 0.01, 0.01, and 0.08, respectively. These indices then decline during the recovery interval. C_{31} αβ/(αβ + ββ) and C_{30} βα/(βα + αβ) ratios exhibit the opposite trend, with lower thermal maturity during the core and the C_{30} βα/(βα + αβ) ratio continuing to decline into the recovery.

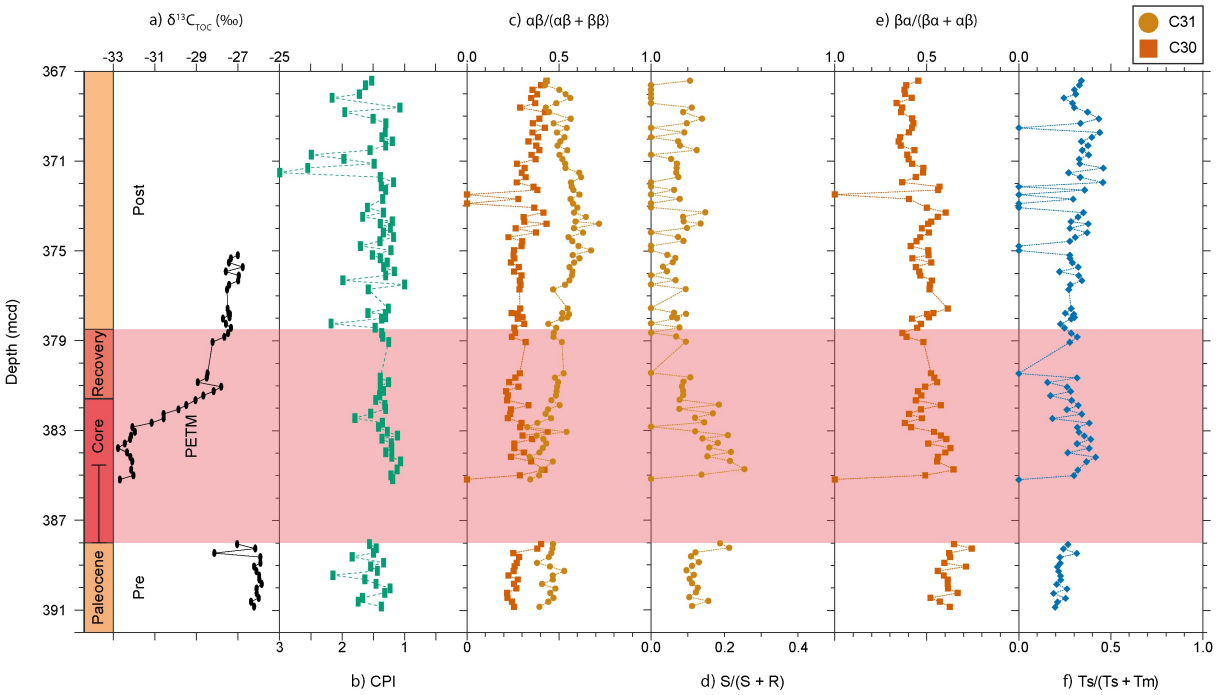

Figure 2: Thermal maturity ratios at ACEX. Note some of the axis are reversed to reflect increasing thermal maturity towards the right. a) bulk sediment $\delta^{13}C$ of total organic carbon ($\delta^{13}C_{TOC}$) (Elling et al., 2019), b) CPI (this study), c) αβ/(αβ + ββ) ratios (this study), d) S/(S + R) ratio (this study), e) βα/(βα + αβ) ratio (this study), and f) $T_s/(T_s + T_m)$ ratio (this study). The PETM interval (including the core and recovery) is highlighted by red shading, and a core gap is present from ~388 to 384.5 mcd (Sluijs et al., 2006)

3.1.2 ODP Site 1172

The apolar fraction contains C_{16} to C_{34} *n*-alkanes and the CPI has a mean value of 2.8. Samples with CPI > 3 (i.e., relatively low thermal maturity), are mostly constrained to the pre-PETM interval (Figure 3). Hopanes range from C_{27} to C_{32} (including αβ, βα, and ββ isomers), and the thermal maturity ratios exhibit a relatively stable trend throughout the sequence. However, C_{31} S/(S + R) ratio slightly increases by 0.09 during the core and into the recovery of the PETM, suggesting potential input of thermally mature organic carbon. C_{30} αβ/(αβ + ββ), C_{31} αβ/(αβ + ββ), and C_{30} βα/(βα + αβ) values present the opposite behaviour, shifting slightly towards thermally immature values during the core of the PETM, by an average of 0.19, 0.22, and 0.07 respectively. During the recovery, all parameters return to more thermally mature values.

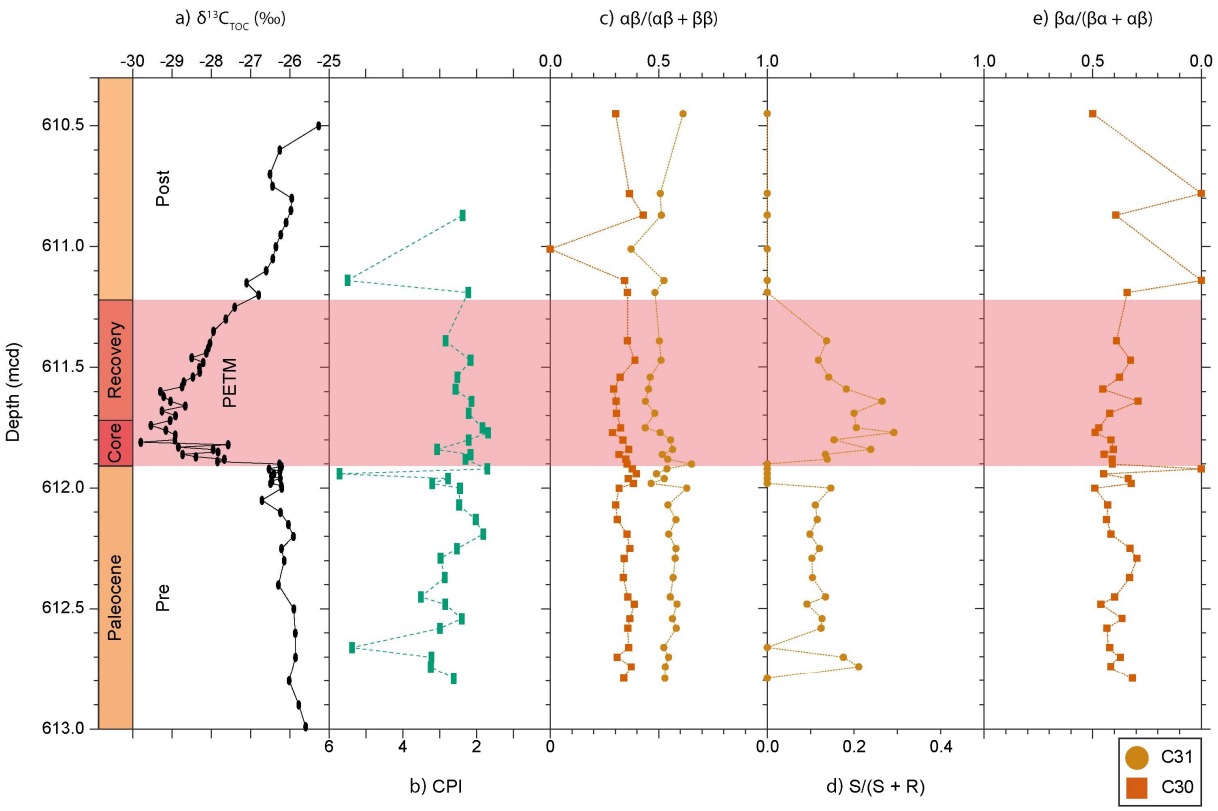

Figure 3: Thermal maturity ratios at ODP Site 1172. Note some of the axis are reversed to reflect increasing thermal maturity towards the right. a) bulk sediment $\delta^{13}C$ of total organic carbon ($\delta^{13}C_{TOC}$) (Sluijs et al., 2011), b) CPI (this study), c) αβ/(αβ + ββ) ratios (this study), d) S/(S + R) ratio (this study), and e) βα/(βα + αβ) ratio (this study). The PETM interval (including the core and recovery) is highlighted by red shading

3.1.3 Kheu River

C_{16} to C_{35} *n*-alkanes were identified in the apolar fraction, in addition to C_{27} to C_{31} hopanes (including αβ, βα, and ββ isomers). Prior to the PETM and during the recovery, the CPI drops below 1, which may suggest input of low-maturity source rocks from carbonates or hypersaline environments. On the other hand, the CPI oscillate drastically between ~1 and ~3 within the lower depths of the core of the PETM (~0–50 cm; Figure 4). This section of high variability is also reflected in the C_{29} αβ/C_{30} αβ and C_{29} βα/(βα + αβ) ratios, suggesting rapid changes in the organic carbon source. However, part of this signal may be biased by greater sampling resolution within the PETM. Overall, the average of all the thermal maturity ratios exhibit lower thermal maturity during the core. In addition, the C_{29} αβ/C_{30} αβ ratio present values > 1 during the

PETM, potentially indicating input from a clay-rich source rock. With the exception of $T_s/(T_s + T_m)$, all of the ratios increase in higher thermal maturity during the recovery to either higher than pre-PETM (i.e., C_{29} αβ/(C_{29} αβ + C_{30} αβ) and $C_{29\text{-}30}$ βα/(βα + αβ) ratios) or near pre-PETM values (i.e., $C_{29\text{-}31}$ αβ/(αβ + ββ) ratio).

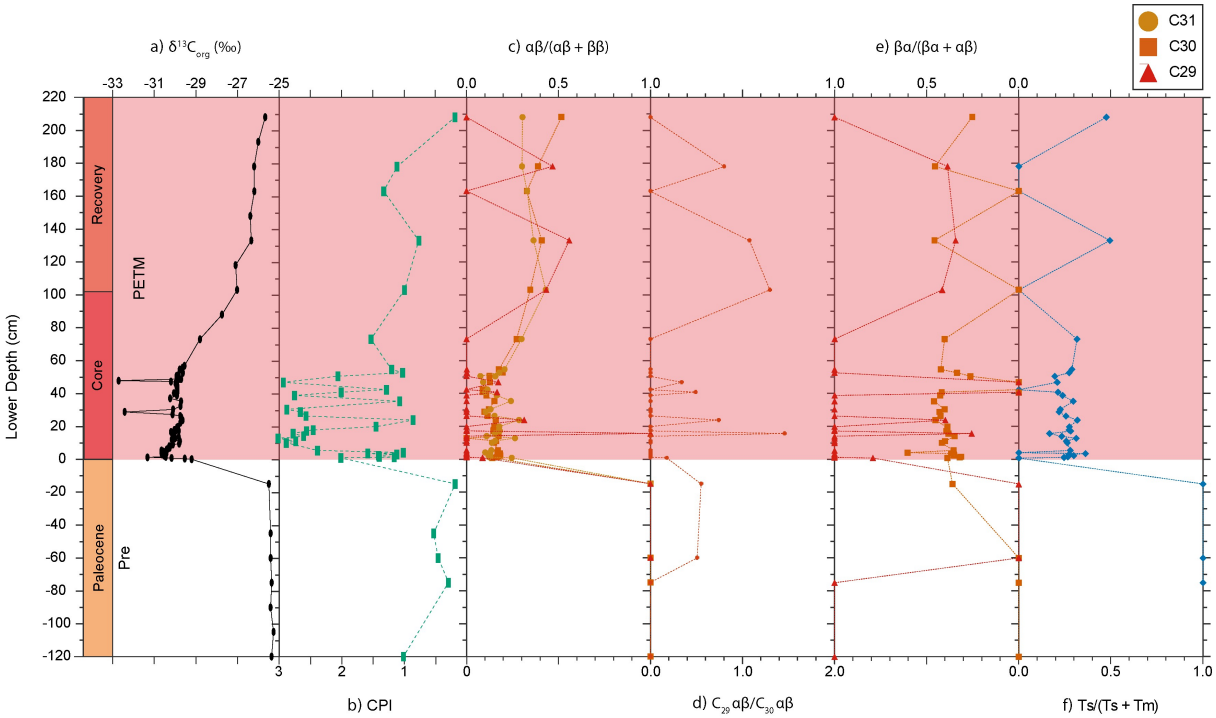

Figure 4: Thermal maturity ratios at Kheu River. Note some of the axis are reversed to reflect increasing thermal maturity towards the right. a) bulk sediment $\delta^{13}C$ of organic carbon ($\delta^{13}C_{org}$) (Dickson et al., 2014), b) CPI (this study), c) αβ/(αβ + ββ) ratios (this study), d) C_{29} αβ/ C_{30} αβ ratio (this study), e) βα/(βα + αβ) ratios (this study), and f) $T_s/(T_s + T_m)$ ratio (this study). The PETM interval (including the core and recovery) is highlighted by red shading

3.1.4 Ancora

The apolar fraction contains C_{15} to C_{34} *n*-alkanes and C_{27} to C_{31} hopanes (including αβ, βα, and ββ isomers). CPI ranges from 1–2.2 and is stable throughout the record (Figure 5). Similarly, $C_{30\text{-}31}$ αβ/(αβ + ββ) values remain relatively constant, albeit exhibiting a very slight decline by an average of 0.01–0.03 (i.e., decreasing thermal maturity). On the other hand, C_{31} S/(S + R) and C_{30} βα/(βα + αβ) values peak towards higher thermal maturity during the core of the PETM. The former presents a drastic shift from an absence of the S configuration to a dominance of R,

368 suggesting potential transient input of thermally mature organic carbon. However, the rise in the
369 two ratios do not occur synchronously, instead C_{31} S/(S + R) values lag behind by ~1.5 mcd.

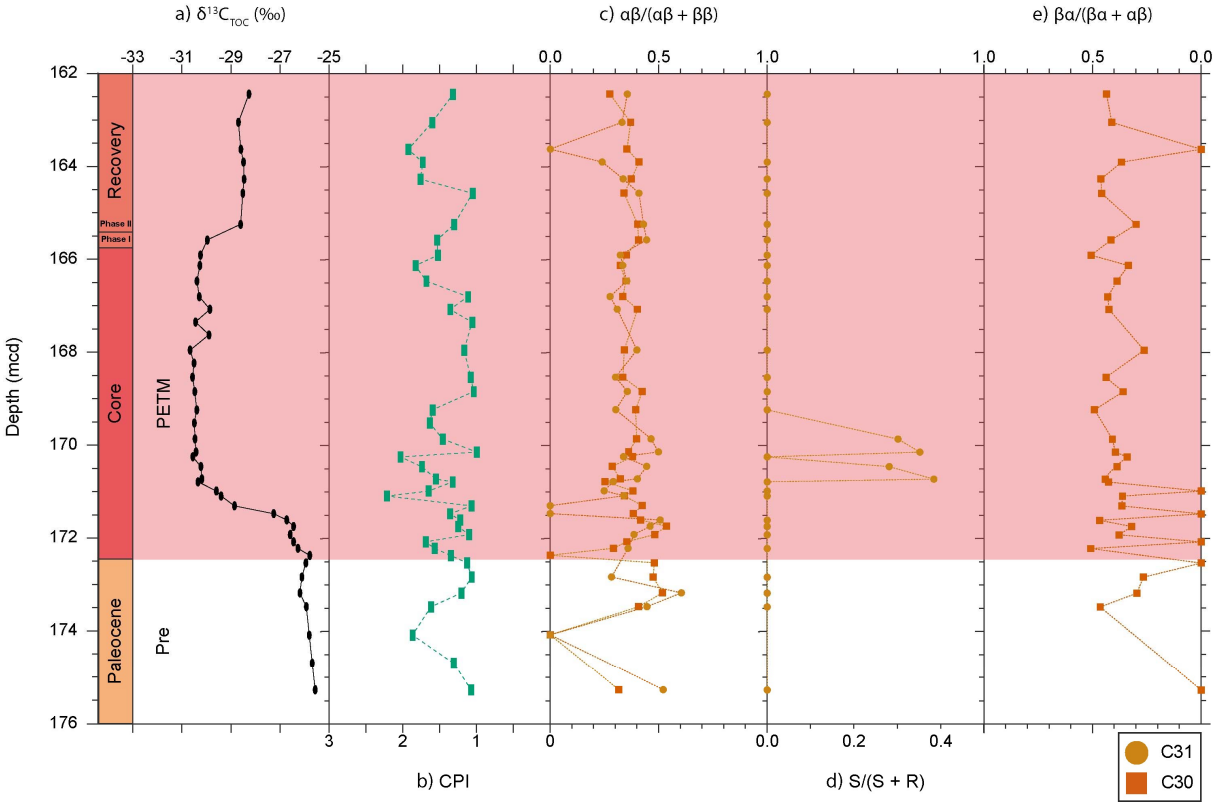

Figure 5: Thermal maturity ratios at Ancora. Note some of the axis are reversed to reflect increasing thermal maturity towards the right. a) bulk sediment $\delta^{13}C$ of total organic carbon ($\delta^{13}C_{TOC}$) (Elling et al., 2019), b) CPI (this study), c) αβ/(αβ + ββ) ratios (this study), d) S/(S + R) ratio (this study), and e) βα/(βα + αβ) ratio (this study). The PETM interval (including the core and recovery) is highlighted by red shading

370 3.1.5 TDP Site 14

371 C_{16} to C_{33} *n*-alkanes and C_{27} to C_{35} hopanes (including αβ, βα, and ββ isomers) were identified in
372 the apolar fraction. The CPI remains > 3 (i.e., low thermal maturity), with the exception of five
373 data points which occur during the core of the PETM (Figure 6). Most noticeable is the large
374 variability in the hopane-based thermal maturity ratios pre-PETM and for the first ~4 m of the
375 core of the PETM. In the upper ~5 m of the core of the PETM, the ratios are more stable and in
376 general agreement. This interval mostly exhibits more thermally mature values than during pre-

PETM section, suggesting a potential shift to an input of thermally mature organic carbon. For example, $C_{29\text{-}31}$ αβ/(αβ + ββ) values are close to its mature endmember of 1.

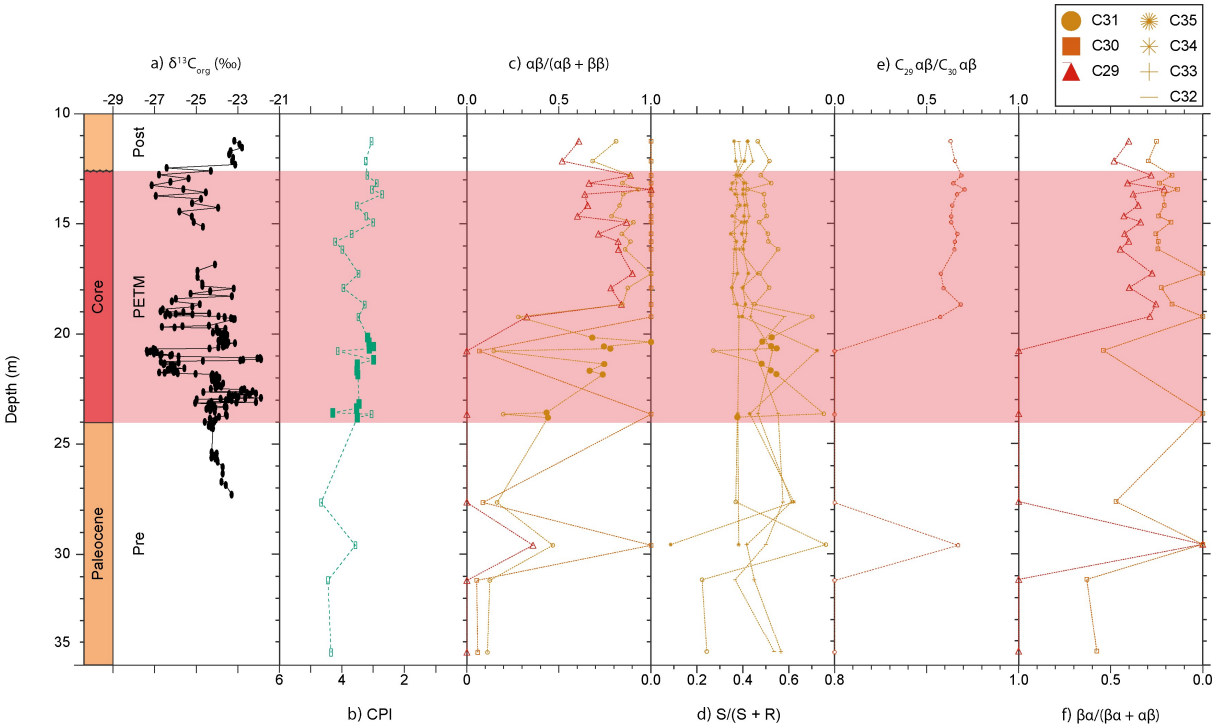

Figure 6: Thermal maturity ratios at TDP Site 14. Note some of the axis are reversed to reflect increasing thermal maturity towards the right. a) bulk sediment $\delta^{13}C$ of organic carbon ($\delta^{13}C_{org}$) (Aze et al., 2014), b) CPI (closed symbols from this study and open symbols from Handley et al., 2012), c) αβ/(αβ + ββ) ratios (closed symbols from this study and open symbols from Handley et al., 2012), d) S/(S + R) ratios (closed symbols from this study and open symbols from Handley et al., 2012), e) C_{29} αβ/ C_{30} αβ ratio (Handley et al., 2012), and f) βα/(βα + αβ) ratios (Handley et al., 2012). The PETM interval (including the core) is highlighted by red shading, and an unconformity truncates the CIE at 12.6 m

3.2 OC_{petro} mass accumulation rates

The OC_{petro} MARs were acquired from all the sites and, following the LSRs, the OC_{petro} MARs were grouped into the key time intervals at each site (see Text S1 in the supporting information). To enable comparison between sites, we calculated the fold change in mean OC_{petro} MARs between pre-PETM and during the PETM (i.e., including the core and recovery of the PETM) (Figure 7). Overall, most of the sites (i.e., ACEX, Kheu River, Ancora, SDB, CamDor, and TDP Site 14) display an increase in OC_{petro} MARs during the PETM. However, the sites with the

386 largest increase are restricted to the mid-latitudes (i.e., Kheu River, Ancora, and SDB). In
387 contrast, ODP Site 1172 exhibits a small decrease in OC_{petro} MAR during the PETM.

388

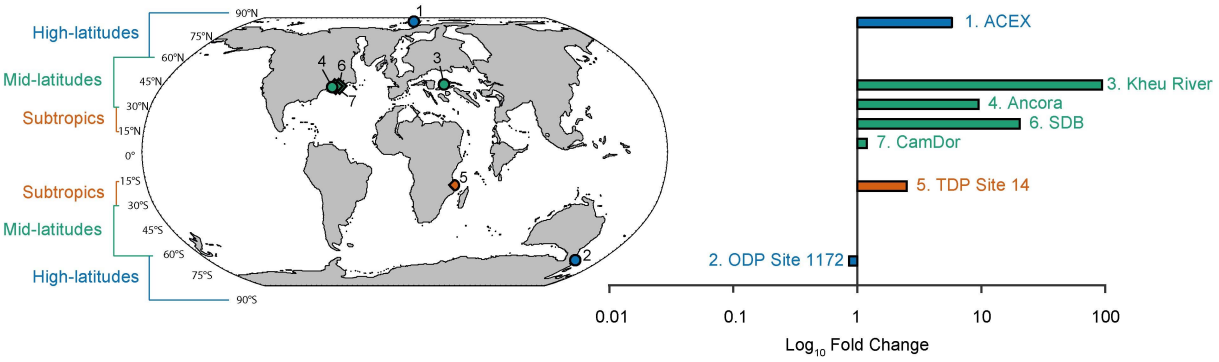

Figure 7: Log_{10} fold change in mean OC_{petro} mass accumulation rates (MARs) between pre-PETM and during the PETM (i.e., including the core and recovery of the PETM). The latitudes are defined as: high (> 60° N/S); mid- (30–60° N/S); and subtropics (15–30° N/S) (see Table S1 in the supporting information)

389 **4 Discussion**

390 4.1 Enhanced OC_{petro} mass accumulation rates in the subtropics and mid-latitudes during
391 the PETM

392 A previous study from Tanzania (TDP Site 14) reported a relative increase in the thermally
393 mature αβ hopane during the PETM (Carmichael et al., 2017; Handley et al., 2012). Here, we
394 present new hopane-based thermal maturity data that reveals rapidly fluctuating values within the
395 first ~4 m of the core of the PETM (Figure 6). Similar patterns were observed in the chain-length
396 distributions of *n*-alkanes, the branched and isoprenoid tetraether (BIT) index, bulk sediment
397 $\delta^{13}C$ of organic carbon ($\delta^{13}C_{org}$), and the *n*-alkane $\delta^{13}C$ record (Aze et al., 2014; Carmichael et
398 al., 2017; Handley et al., 2008, 2012). The latter two was previously suggested to reflect episodic
399 reworking of older (pre-PETM) material rather than changes in the atmospheric carbon reservoir
400 (Figure 6; Aze et al., 2014; Handley et al., 2008). The hopane-based thermal maturity ratios
401 within this study confirms this variable delivery of organic carbon sources, from OC_{bio} to OC_{petro}.
402 In contrast, the upper ~5 m of the core of the PETM exhibits more stability in the hopane-based
403 thermal maturity ratios (Carmichael et al., 2017; Handley et al., 2012), $\delta^{13}C_{org}$values, and *n*-
404 alkane $\delta^{13}C$ values (Aze et al., 2014; Handley et al., 2008). The hopane-based thermal maturity

ratios also present higher thermal maturity, indicating a switch from an episodic to persistent delivery of OC_{petro} (Carmichael et al., 2017; Handley et al., 2012). During the PETM, the overall increase in thermally mature hopanes in addition to the LSR drives the OC_{petro} MARs to rise by an average of $8x10^{-3}$ gC cm^2 kyr^{-1} (Figure 7). This enhanced OC_{petro} MAR is consistent with evidence of a shift from predominantly marine organic carbon to a terrestrial organic carbon source (e.g., an increase in the abundance of long-chain *n*-alkanes produced by vascular plants and brGDGTs produced by soil bacteria; Carmichael et al., 2017; Handley et al., 2008, 2012). Whilst there is greater LSR and terrigenous sediment during the PETM, TOC values declined. This drop was attributed to the larger contributions of clay (Handley et al., 2012). Evidence includes an abundance of kaolinite, suggestive of intensified physical erosion (John et al., 2012), and high Li/Al combined with low Na/Al, suggestive of exhumation of older weathered clay. These additional proxies also suggest processes that support an increase the mobilisation and accumulation of OC_{petro} during the PETM.

Similar to Tanzania, Ancora exhibits an increase in the average OC_{petro} MARs (by $2x10^{-2}$ gC cm^2 kyr^{-1}) during the PETM. This value falls within the average OC_{petro} MARs estimated at two other sites from the Atlantic Coastal Plain (i.e., $6x10^{-2}$ gC cm^2 kyr^{-1} SDB and $8x10^{-3}$ gC cm^2 kyr^{-1} CamDor; Figure 7). The higher OC_{petro} MAR is largely driven by a shift in LSR from 0.8 cm kyr^{-1} (pre-PETM) to 11.28 cm kyr^{-1} (PETM) (Table 1; Stassen et al., 2012). Evidence for terrestrial input to the Atlantic Coastal Plain during the PETM includes a higher abundance of kaolinite (Gibson et al., 2000), detrital magnetic minerals (Kopp et al., 2009), charcoal, seed pods, and terrestrial spores (Self-Trail et al., 2017). In addition, there is an increase in the terrestrial aquatic ratio (TAR; Bourbonniere & Meyers, 1996; Lyons et al., 2019). Indirect evidence includes changes in the marine microfossil assemblage towards benthic foraminifera (Self-Trail et al., 2017) and dinoflagellates (Sluijs & Brinkhuis, 2009) that can tolerate brackish water with high sediment input (Self-Trail et al., 2017). However, with the exception of the abrupt peaks of C_{31} S/(S + R) at ~169–171 mcd and C_{30} βα/(βα + αβ) at ~171–173 mcd, the thermal maturity ratios at Ancora are relatively stable compared to SDB and CamDor (Figure 5; Lyons et al., 2019). Furthermore, SDB and CamDor are characterised by a 6 ‰ increase in $\delta^{13}C_{org}$ values during the PETM (Lyons et al., 2019), which was argued to represent reworking of older (pre-PETM)

435 material and not an increase in primary production (Lyons et al., 2019) This ^{13}C enrichment is
436 not observed at Ancora (Figure 5; Elling et al., 2019).

437

438 The average OC_{petro} MAR at Kheu River exhibits an increase (by $3x10^{-2}$ gC cm^2 kyr^{-1}) during the
439 PETM (Figure 7), driven by an order-of-magnitude rise in TOC values from an average
440 background level of ~0.1 % (pre- and post-PETM) to ~4.4 % (Dickson et al., 2014). However, in
441 contrast to the sites discussed thus far, Kheu River thermal maturity ratios shift to immature
442 values during the core of the PETM (Figure 4). During the PETM, the *n*-alkane distribution is
443 dominated by long-chain homologues characteristic of vascular plants (Dickson et al., 2014). It
444 can therefore be argued that the shift observed in the thermal maturity ratios is mostly due to
445 enhanced input of the OC_{bio} (i.e., immature hopanes such as ββ isomers) transported from land,
446 although in situ production cannot be dismissed. In addition, the $\delta^{13}C_{org}$ record does not present
447 ^{13}C enrichment during the PETM (Figure 4; Dickson et al., 2014). However, an increase in the
448 Chemical Index of Alteration (CIA) and spike in Ti/Al during the PETM not only corroborates
449 terrestrial input but possibly erosion of older (pre-PETM) material (Dickson et al., 2014). As
450 such, both OC_{petro} and (to a larger extent) OC_{bio} likely contributed. Therefore, this study
451 highlights the need to quantify OC_{bio}, as any carbon sequestered via OC_{bio} burial may negate CO_2
452 released via enhanced OC_{petro} oxidation (e.g., Bowen & Zachos, 2010; John et al., 2008; Kaya et
453 al., 2022; Papadomanolaki et al., 2022; Sluijs, Röhl, et al., 2008). Indeed, this was demonstrated
454 to have occurred during the Holocene (e.g., Galy et al., 2015; Hilton et al., 2015; Kao et al.,
455 2014). In conclusion, the subtropical and mid-latitude sites all exhibit an increase in OC_{petro}
456 MAR during the PETM, and thus may provide an additional source of CO_2. However,
457 understanding whether the Kheu River region was a net carbon source or sink requires further
458 investigations.

459 4.2 Stable organic carbon sources in the high-latitudes during the PETM

460 In the subtropics and mid-latitudes, average OC_{petro} MAR increased between $8x10^{-3}$ to $6x10^{-2}$ gC
461 cm^2 kyr^{-1} during the PETM for a given site (see Section 4.1). In the high-latitudes, OC_{petro} MARs
462 in the Arctic (ACEX) and the southwest Pacific Ocean (ODP Site 1172) either increase (by $7x10^{-2}$
463 gC cm^2 kyr^{-1}) or decrease (by $3x10^{-4}$ gC cm^2 kyr^{-1}), respectively (Figure 7). The decline
464 observed at ODP Site 1172 is due to a drop in TOC values and LSRs. The marked rise at ACEX

is mostly driven by a peak in TOC values, from a minimum of 1.3 % (pre-PETM) to a maximum of 4.9 % (core PETM) (Elling et al., 2019). Absolute abundances of palynomorphs from ACEX suggest that the high TOC is a mixture of marine and terrestrial organic matter (Sluijs, Röhl, et al., 2008). However, both sites, with the exception of the C_{31} S/(S + R) ratio at ODP Site 1172, have thermal maturity ratios that are very stable throughout the record (Figure 2–3). This indicates that although the supply of organic carbon increased during the PETM, the organic carbon source did not distinctly change. Intriguingly, there is an antiphase between C_{30} αβ/(αβ + ββ) and C_{31} αβ/(αβ + ββ) at ACEX, perhaps suggesting subtle changes in the organic carbon source during the PETM. Decoupling between the C_{30} and C_{31} indices could be due to a greater input of acidic peats, which are dominated by C_{31} αβ hopanes but lack abundant C_{30} αβ isomers (Inglis et al., 2018). The contribution of acidic peats at ACEX has also been inferred from brGDGTs (Sluijs et al., 2020).

4.3 Climate exerts primary control on OC_{petro} mobilisation during the PETM

Various factors may explain why shallow marine sediments are characterised by enhanced delivery of OC_{petro} during the PETM. Modern observations have identified a strong link between rainfall and efficient erosion/transfer of organic carbon from land-to-sea (e.g., T. I. Eglinton et al., 2021; Hilton, 2017). In the subtropics, evidence for changes in the hydrological cycle during the PETM are scarce. Previous work at TDP Site 14 revealed that the hydrogen isotope of *n*-alkanes ($\delta^2H_{n\text{-alkanes}}$) increased during the PETM, which was inferred to represent a shift towards more arid climate conditions (Carmichael et al., 2017; Handley et al., 2008). Enhanced aridity could lead to minimal vegetation cover, hindering soil development, and maximising the potential for erosion and mobilisation of OC_{petro} (e.g., Hilton et al., 2008; Leithold et al., 2006). Furthermore, large fluctuations in $\delta^2H_{n\text{-alkanes}}$ values may indicate oscillations between dry and wet climate states and/or an increase in extreme precipitation events (Carmichael et al., 2017; Handley et al., 2008). Modelling studies over subtropical Africa during the PETM further support the latter (Carmichael et al., 2018). Episodic and intense rainfall on a landscape prone to erosion would explain the highly variable delivery of different organic carbon sources, as shown by the hopane-based thermal maturity data (this study), $\delta^{13}C_{org}$values, and *n*-alkane $\delta^{13}C$ values (Aze et al., 2014; Handley et al., 2008).

Analogous to TDP Site 14, Kheu River also exhibits high variability in the thermal maturity ratios (e.g., CPI, C_{29} αβ/C_{30} αβ, and C_{29} βα/(βα + αβ); this study), chain-length distributions of *n*-alkanes, BIT index, grain-size, and CIA during the PETM (Dickson et al., 2014). These features are consistent with episodic changes in precipitation, although some of the pulses at Kheu River have been argued to correlate to brief intervals of marine transgression (Shcherbinina et al., 2016). There are multiple lines of evidences associating other mid-latitude sites with increased transient and extreme rainfall events during the PETM. For example, the deposition of conglomerates in the Pyrenees (Chen et al., 2018; Schmitz & Pujalte, 2003, 2007) and changes in paleosol weathering indices and/or the abundance and composition of nodules in the Bighorn Basin (e.g., Kraus et al., 2013; Kraus & Riggins, 2007). There is also evidence for greater freshwater runoff in the Atlantic Coastal Plain (i.e., Ancora, SDB, and CamDor) during the PETM, with the development of a river-dominated shelf referred to as the "Appalachian Amazon" (Doubrawa et al., 2022; Kopp et al., 2009; Self-Trail et al., 2017). This is consistent with high-resolution climate models that suggest the western Atlantic region was dominated by an increase in extratropical cyclones and more extreme rainfall events (Kiehl et al., 2021; Rush et al., 2021; Shields et al., 2021). Although the hydrological cycle likely exerted a first-order control on the mobilisation of terrestrial organic carbon, other ecological and/or geologic controls could have also been important. For example, the dominance of OC_{bio} at Kheu River may reflect abundant vegetation cover (e.g., Goñi et al., 2013). On the other hand, the dominance of OC_{petro} at TDP Site 14 may reflect greater availability of OC_{petro}-rich rock and/or exacerbated erosion of OC_{petro} caused by limited soil and vegetation (e.g., Hilton et al., 2011).

Model simulations also indicate an increase in precipitation in the high-latitudes for a PETM-type warming event (e.g., Carmichael et al., 2016; Cramwinckel et al., 2023; Winguth et al., 2010). Proxies also reconstruct northern and southern high-latitudes to be wetter at the onset of the PETM (e.g., evidence from palynomorphs (Korasidis et al., 2022; Sluijs et al., 2006), fossilised plants (Harding et al., 2011), hydrogen isotopes of *n*-alkanes ($\delta^2H_{n\text{-alkanes}}$; Pagani et al., 2006), and clay-mineralogy (Dypvik et al., 2011; Kaiho et al., 1996; Robert & Kennett, 1994)). Yet, both high-latitude sites (i.e., ACEX and ODP Site 1172) exhibit a relatively stable source of organic carbon during the PETM. This suggests that changes in seasonality and extreme precipitation events (alongside overall wetter conditions) are required to mobilise OC_{petro} (see

section 4.1). Alternatively, there may be other feedback mechanisms and/or more regional controls beyond the hydrological cycle. In modern systems, local geomorphic processes play a strong role in regulating OC_{petro} transport from land-to-sea (e.g., Hilton & West, 2020). However, tectonic activity is hard to constrain in deep-time. Variability in OC_{petro} MARs could also be attributed to changes in sea level during the PETM. Indeed, various studies have suggested marine transgression during the PETM, including: ACEX (Sluijs et al., 2006); ODP Site 1172 (Sluijs et al., 2011); Kheu River (Shcherbinina et al., 2016); the Atlantic Coastal Plain (John et al., 2008); and elsewhere (Sluijs, Brinkhuis, et al., 2008 and references therein). Although sea level rise is expected to reduce the supply of terrestrial organic carbon into the marine real, this is rarely observed (e.g., Sluijs et al., 2014) and most PETM sites are characterised by enhanced terrigenous material during the PETM (Carmichael et al., 2017 and references therein).

4.4 Timing and implications for CO_2 release during the PETM

Enhanced OC_{petro} delivery was suggested to have occurred ~10–20 kyrs after the onset of the PETM (i.e., within the body of the CIE) by Lyons et al. (2019). Here we confirm that elevated OC_{petro} MARs occurred within the core of the PETM at several other sites (i.e., ACEX, Kheu River, Ancora; Figure 8). However, the exact timing within the core (i.e., onset or body) cannot be determined due to the lack of robust age constraints. The sites where the recovery phases were defined (i.e., ACEX, Kheu River, Ancora, and SDB), enables insight into whether enhanced OC_{petro} MARs continued after the body of the CIE or recovered to pre-PETM values. Interestingly, at both Ancora and SDB, median OC_{petro} MARs are higher than the core of the PETM in Phase II and I, respectively (Figure 8). Although an increase in OC_{petro} MAR during the recovery is not observed at ACEX and Kheu River, values do not return to pre-PETM levels. This suggests that at certain localities, terrestrial organic carbon cycle perturbations continued into the recovery phase. If this OC_{petro} was oxidised, it may provide an additional source of CO_2 during the recovery.

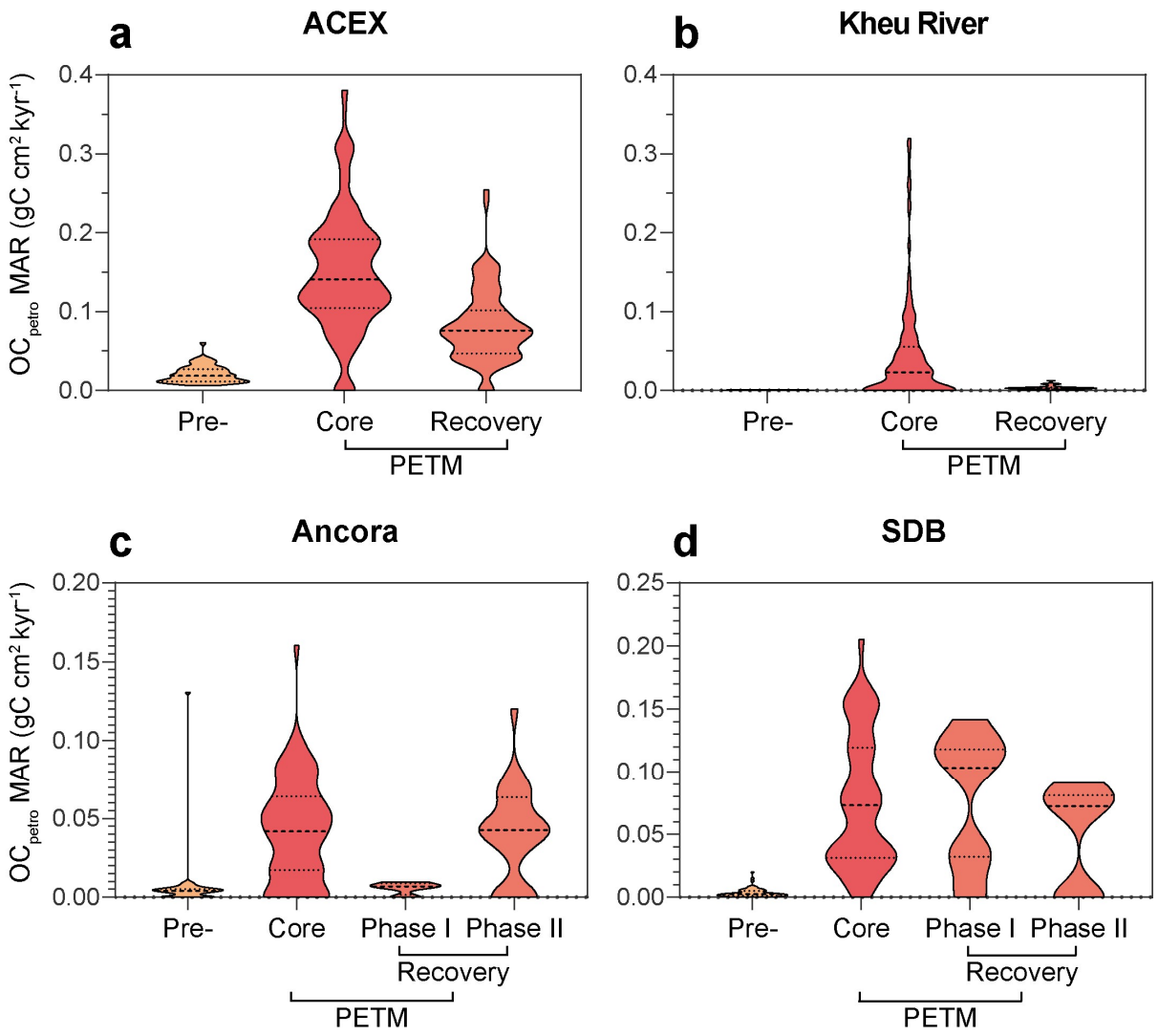

Figure 8: Violin plots of OC_{petro} MARs (gC cm^{-} kyr^{-1}) for the defined time intervals of site (a) ACEX, (b) Kheu River, (c) Ancora, and (d) SDB. The thick dashed line represents the median and the thin dashed line extends from the 25th to 75th percentiles.

Overall, Lyons et al. (2019) inferred between 10^2 and 10^4 PgC was released as CO_2 globally due to oxidation of OC_{petro} during the PETM. This assumed that the study sites (i.e., SDB, CamDor, and TDP Site 14) are globally representative. However, this study demonstrates that an increase in OC_{petro} MARs was mostly restricted to the subtropics and mid-latitudes. In addition, the maximum value of 10^4 PgC assumed that 85 % of OC_{petro} is oxidised. However, increased erosion of clastic sediments can aid the preservation of OC_{petro} (e.g., Bouchez et al., 2014; Burdige, 2007). Furthermore, intense precipitation events (characteristic of the subtropics and mid-latitudes; e.g., Carmichael et al., 2017; Handley et al., 2008; Kiehl et al., 2021; Kraus et al.,

559 2013; Kraus & Riggins, 2007; Rush et al., 2021; Schmitz & Pujalte, 2003, 2007; Shields et al.,
560 2021) may reduce the transfer time of OC_{petro} from source to sink, thereby reducing the
561 possibility for oxidation (e.g., Hilton et al., 2011). However, it is important to consider that
562 shallow marine sites will likely integrate an expansive catchment area, which incorporate slow
563 meandering rivers as well as steep mountainous rivers. In the former system, the extent of OC_{petro}
564 oxidised could be as high as ~90 % (e.g., Bouchez et al., 2010; Galy et al., 2008). This is
565 especially likely at sites where large freshwater input was evident, such as the Atlantic Coastal
566 Plain (Doubrawa et al., 2022; Kopp et al., 2009; Self-Trail et al., 2017). Future work on paleo-
567 digital elevation models may further help elucidate sediment routing systems during the PETM
568 (Lyster et al., 2020). In conclusion, this study demonstrates that although oxidation of OC_{petro}
569 likely contributed additional CO_2 during the PETM, global estimates may be lower than
570 previously inferred. We also demonstrate that CO_2 release may have continued into the recovery
571 of the PETM, suggesting that other feedback mechanisms (e.g., OC_{bio} burial) were necessary to
572 aid in the recovery of the Earth's climate system.

573 **5 Conclusion**

574 Here, we use a multi-biomarker approach to reconstruct the mobilisation of petrogenic organic
575 carbon (OC_{petro}) during the PETM. We find widespread evidence for enhanced OC_{petro} mass
576 accumulation rates (MARs) in the subtropics and mid-latitudes during the PETM. In this region,
577 we argue that extreme rainfall events exacerbated erosion, mobilisation, and burial of OC_{petro} in
578 the marine realm. In addition, we demonstrate that OC_{petro} MARs persisted into the recovery
579 phase of the PETM. However, the high-latitude sites do not exhibit a strong shift in the source of
580 organic carbon. This may be due to a more stable hydrological regime and/or additional controls
581 such as geomorphic processes or sea level change. Overall, OC_{petro} oxidation likely acted as an
582 additional source of CO_2 during the PETM . However, further work is needed to determine the
583 exact contributions of OC_{petro} as a positive feedback mechanism during the PETM and other
584 transient warming events.

585 **Acknowledgment**

586 G.N. Inglis is supported by a GCRF Royal Society Dorothy Hodgkin Fellowship
587 (DHF\R1\191178) with additional support via the Royal Society (RF\ERE\231019,
588 RF\ERE\210068). E.H. Hollingsworth acknowledges funding from a NERC (Grant

NE/S007210). This research used samples provided by the Ocean Drilling Program (ODP) and the International Ocean Drilling Program (IODP). F.J. Elling is supported by Deutsche Forschungsgemeinschaft grant (441217575) and A. Pearson was supported by the US National Science Foundation (Grant OCE-1843285). We thank Katiana Doeana and Susan Carter at Havard University for laboratory assistance. For TDP Site 14 samples, we thank colleagues in the Tanzanian Drilling Project, and especially those from the Tanzanian Petroleum Development Corporation. Partial funding for M.P.S Badger was provided by NERC grant (NE/H006273/1). For Kheu River samples, we thank E.A. Shcherbinina, Y. Gavrilov, and A.J. Dickson who is supported by UKRI Frontier Research Grant (EP/X022080/1). We thank the NERC Life Sciences Mass Spectrometry Facility for technical support of the GC-MS and NERC for partial funding of the mass spectrometry facilities at Bristol (R8/H10/63). N.M. Papadomanolaki acknowledges funding from The Netherlands Earth System Science Center (NESSC), financially supported by the Ministry of Education, Culture and Science (OCW). We thank Arnold van Dijk for analytical assistance.

Conflict of Interest

The authors declare no conflicts of interest relevant to this study.

Data Availability Statement

The processed data used in this study are available at OSF and associated with a CC-By Attribution 4.0 International license (Hollingsworth, 2023).

Author contributions:

Conceptualization: E. H. Hollingsworth, G. N. Inglis

Investigation: E. H. Hollingsworth, F. J. Elling, M. P. S. Badger, A. J. Dickson, R. L. Rees-Owen, N. M. Papadomanolaki, G. N. Inglis

Resources: F. J. Elling, A. Pearson

Visualisation: E. H. Hollingsworth

Writing – original draft: E. H. Hollingsworth

Writing – review & editing: F. J. Elling, M. P. S. Badger, R. D. Pancost, A. J. Dickson, N. M. Papadomanolaki, A. Pearson, A. Sluijs, A. A. Baczynski, G. L. Foster, J. H. Whiteside, G. N. Inglis

Project administration: E. H. Hollingsworth, G. N. Inglis

Supervision: G. L. Foster, J. H. Whiteside, G. N. Inglis

References

Aze, T., Pearson, P. N., Dickson, A. J., Badger, M. P. S., Bown, P. R., Pancost, R. D., Gibbs, S. J., Huber, B. T., Leng, M. J., Coe, A. L., Cohen, A. S., & Foster, G. L. (2014). Extreme warming of tropical waters during the Paleocene – Eocene Thermal Maximum. *Geology*, *42*(9), 739–742. https://doi.org/10.1130/G35637.1

Berhe, A. A., Harte, J., Harden, J. W., & Torn, M. S. (2007). The Significance of the Erosion-induced Terrestrial Carbon Sink. *BioScience*, *57*(4), 337–346. https://doi.org/10.1641/B570408

Berner, R. A., Lasaga, A. C., & Garrels, R. M. (1983). The carbonate-silicate geochemical cycle and its effect on atmospheric carbon dioxide over the past 100 million years. *American Journal of Science*, *283*(7), 641–683. https://doi.org/10.2475/ajs.283.7.641

Bianchi, T. S., Cui, X., Blair, N. E., Burdige, D. J., Eglinton, T. I., & Galy, V. (2018). Centers of organic carbon burial and oxidation at the land-ocean interface. *Organic Geochemistry*, *115*, 138–155. https://doi.org/10.1016/j.orggeochem.2017.09.008

Blair, N. E., Leithold, E. L., Ford, S. T., Peeler, K. A., Holmes, J. C., & Perkey, D. W. (2003). The persistence of memory: The fate of ancient sedimentary organic carbon in a modern sedimentary system. *Geochimica et Cosmochimica Acta*, *67*(1), 63–73. https://doi.org/10.1016/S0016-7037(02)01043-8

Bolle, M. P., Pardo, A., Hinrichs, K. U., Adatte, T., Von Salis, K., Burns, S., Keller, G., & Muzylev, N. (2000). The Paleocene-Eocene transition in the marginal northeastern Tethys (Kazakhstan and Uzbekistan). *International Journal of Earth Sciences*, *89*(2), 390–414. https://doi.org/10.1007/s005310000092

Bouchez, J., Beyssac, O., Galy, V., Gaillardet, J., France-lanord, C., Maurice, L., & Moreira-turcq, P. (2010). Oxidation of petrogenic organic carbon in the Amazon floodplain as a

source of atmospheric CO2. *Geology*, *38*(3), 255–258. https://doi.org/10.1130/G30608.1

Bouchez, J., Galy, V., Hilton, R. G., Gaillardet, J. Ô., Moreira-Turcq, P., Pérez, M. A., France-Lanord, C., & Maurice, L. (2014). Source, transport and fluxes of Amazon River particulate organic carbon: Insights from river sediment depth-profiles. *Geochimica et Cosmochimica Acta*, *133*, 280–298. https://doi.org/10.1016/j.gca.2014.02.032

Bourbonniere, R. A., & Meyers, P. A. (1996). Sedimentary geolipid records of historical changes in the watersheds and productivities of Lakes Ontario and Erie. *Limnology and Oceanography*, *41*(2), 352–359. https://doi.org/10.4319/lo.1996.41.2.0352

Bowen, G. J. (2013). Up in smoke: A role for organic carbon feedbacks in Paleogene hyperthermals. *Global and Planetary Change*, *109*, 18–29. https://doi.org/10.1016/j.gloplacha.2013.07.001

Bowen, G. J., Bralower, T. J., Delaney, M. L., Dickens, G. R., Kelly, D. C., Koch, P. L., Kump, L. R., Meng, J., Sloan, L. C., Thomas, E., Wing, S. L., & Zachos, J. C. (2006). Eocene hyperthermal event offers insight into greenhouse warming. *Eos*, *87*(17), 165–169. https://doi.org/10.1029/2006eo170002

Bowen, G. J., & Zachos, J. C. (2010). Rapid carbon sequestration at the termination of the Palaeocene-Eocene Thermal Maximum. *Nature Geoscience*, *3*, 866–869. https://doi.org/10.1038/ngeo1014

Bray, E. E., & Evans, E. D. (1961). Distribution of n-paraffins as a clue to recognition of source beds. *Geochimica et Cosmochimica Acta*, *22*(1), 2–15. https://doi.org/10.1016/0016-7037(61)90069-2

Burdige, D. J. (2007). Preservation of organic matter in marine sediments: Controls, mechanisms, and an imbalance in sediment organic carbon budgets? *Chemical Reviews*, *107*(2), 467–485. https://doi.org/10.1021/cr050347q

Bush, R. T., & McInerney, F. A. (2013). Leaf wax n-alkane distributions in and across modern plants: Implications for paleoecology and chemotaxonomy. *Geochimica et Cosmochimica Acta*, *117*, 161–179. https://doi.org/10.1016/j.gca.2013.04.016

Caldeira, K., & Berner, R. A. (1997). The need for mass balance and feedback in the geochemical carbon. *Geology*, *25*(10), 955–953. https://doi.org/10.1130/0091-7613(1997)025<0955

Carmichael, M. J., Inglis, G. N., Badger, M. P. S., Naafs, B. D. A., Behrooz, L., Remmelzwaal,

677 S., Monteiro, F. M., Rohrssen, M., Farnsworth, A., Buss, H. L., Dickson, A. J., Valdes, P.
678 J., Lunt, D. J., & Pancost, R. D. (2017). Hydrological and associated biogeochemical
679 consequences of rapid global warming during the Paleocene-Eocene Thermal Maximum.
680 *Global and Planetary Change*, *157*, 114–138.
681 https://doi.org/10.1016/j.gloplacha.2017.07.014
682 Carmichael, M. J., Lunt, D. J., Huber, M., Heinemann, M., Kiehl, J., LeGrande, A., Loptson, C.
683 A., Roberts, C. D., Sagoo, N., Shields, C., Valdes, P. J., Winguth, A., Winguth, C., &
684 Pancost, R. D. (2016). A model-model and data-model comparison for the early Eocene
685 hydrological cycle. *Climate of the Past*, *12*(2), 455–481. https://doi.org/10.5194/cp-12-455-
686 2016
687 Carmichael, M. J., Pancost, R. D., & Lunt, D. J. (2018). Changes in the occurrence of extreme
688 precipitation events at the Paleocene – Eocene thermal maximum. *Earth and Planetary*
689 *Science Letters*, *501*, 24–36. https://doi.org/10.1016/j.epsl.2018.08.005
690 Chen, C., Guerit, L., Foreman, B. Z., Hassenruck-Gudipati, H. J., Adatte, T., Honegger, L.,
691 Perret, M., Sluijs, A., & Castelltort, S. (2018). Estimating regional flood discharge during
692 Palaeocene-Eocene global warming. *Scientific Reports*, *8*(1), 1–8.
693 https://doi.org/10.1038/s41598-018-31076-3
694 Clark, K. E., Hilton, R. G., West, A. J., Robles Caceres, A., Gröcke, D. R., Marthews, T. R.,
695 Ferguson, R. I., Asner, G. P., New, M., & Malhi, Y. (2017). Erosion of organic carbon from
696 the Andes and its effects on ecosystem carbon dioxide balance. *Journal of Geophysical*
697 *Research: Biogeosciences*, *122*(3), 449–469. https://doi.org/10.1002/2016JG003615
698 Clark, K. E., Stallard, R. F., Murphy, S. F., Scholl, M. A., González, G., Plante, A. F., &
699 McDowell, W. H. (2022). Extreme rainstorms drive exceptional organic carbon export from
700 forested humid-tropical rivers in Puerto Rico. *Nature Communications*, *13*(1), 1–8.
701 https://doi.org/10.1038/s41467-022-29618-5
702 Cramwinckel, M. J., Burls, N. J., Fahad, A. A., Knapp, S., West, C. K., Reichgelt, T.,
703 Greenwood, D. R., Chan, W. Le, Donnadieu, Y., Hutchinson, D. K., de Boer, A. M.,
704 Ladant, J. B., Morozova, P. A., Niezgodzki, I., Knorr, G., Steinig, S., Zhang, Z., Zhu, J.,
705 Feng, R., … Inglis, G. N. (2023). Global and Zonal-Mean Hydrological Response to Early
706 Eocene Warmth. *Paleoceanography and Paleoclimatology*, *38*(6), 1–21.
707 https://doi.org/10.1029/2022PA004542

Deconto, R. M., Galeotti, S., Pagani, M., Tracy, D., Schaefer, K., Zhang, T., Pollard, D., & Beerling, D. J. (2012). Past extreme warming events linked to massive carbon release from thawing permafrost. *Nature*, *484*(7392), 87–91. https://doi.org/10.1038/nature10929

Dickens, G. R. (2011). Down the Rabbit Hole: Toward appropriate discussion of methane release from gas hydrate systems during the Paleocene-Eocene thermal maximum and other past hyperthermal events. *Climate of the Past*, *7*(3), 831–846. https://doi.org/10.5194/cp-7-831-2011

Dickens, G. R., Castillo, M. M., & Walker, J. C. G. (1997). A blast of gas in the latest Paleocene: Simulating first-order effects of massive dissociation of oceanic methane hydrate. *Geology*, *25*(3), 259–262. https://doi.org/10.1130/0091-7613(1997)025<0259:ABOGIT>2.3.CO;2

Dickens, G. R., O'Neil, J. R., Rea, D. K., & Owen, R. M. (1995). Dissociation of oceanic methane hydrate as a cause of the carbon isotope excursion at the end of the Paleocene. *Paleoceanography*, *10*(6), 965–971. https://doi.org/10.1029/95PA02087

Dickson, A. J., Rees-owen, R. L., März, C., Coe, A. L., Cohen, A. S., Pancost, R. D., Taylor, K., & Shcherbinina, E. (2014). The spread of marine anoxia on the northern Tethys margin during the Paleocene-Eocene Thermal Maximum. *Paleoceanography*, *29*(6), 471–488. https://doi.org/10.1002/2014PA002629.Received

Diefendorf, A. F., & Freimuth, E. J. (2017). Extracting the most from terrestrial plant-derived n-alkyl lipids and their carbon isotopes from the sedimentary record: A review. *Organic Geochemistry*, *103*, 1–21. https://doi.org/10.1016/j.orggeochem.2016.10.016

Doubrawa, M., Stassen, P., Robinson, M. M., Babila, T. L., Zachos, J. C., & Speijer, R. P. (2022). Shelf Ecosystems Along the U.S. Atlantic Coastal Plain Prior to and During the Paleocene-Eocene Thermal Maximum: Insights Into the Stratigraphic Architecture. *Paleoceanography and Paleoclimatology*, *37*(10), 1–21. https://doi.org/10.1029/2022PA004475

Dypvik, H., Riber, L., Burca, F., Rüther, D., Jargvoll, D., Nagy, J., & Jochmann, M. (2011). The Paleocene-Eocene thermal maximum (PETM) in Svalbard - clay mineral and geochemical signals. *Palaeogeography, Palaeoclimatology, Palaeoecology*, *302*(3–4), 156–169. https://doi.org/10.1016/j.palaeo.2010.12.025

Eglinton, G., & Hamilton, R. J. (1967). Leaf epicuticular waxes. *Science*, *156*(3780), 1322–1335. https://doi.org/10.1126/science.156.3780.1322

739 Eglinton, T. I., Galy, V. V., Hemingway, J. D., Feng, X., Bao, H., Blattmann, T. M., Dickens, A.
740 F., Gies, H., Giosan, L., Haghipour, N., Hou, P., Lupker, M., McIntyre, C. P., Montluçon,
741 D. B., Peucker-Ehrenbrink, B., Ponton, C., Schefuß, E., Schwab, M. S., Voss, B. M., …
742 Zhao, M. (2021). Climate control on terrestrial biospheric carbon turnover. *Proceedings of*
743 *the National Academy of Sciences of the United States of America*, *118*(8).
744 https://doi.org/10.1073/pnas.2011585118
745 Elling, F. J., Gottschalk, J., Doeana, K. D., Kusch, S., Hurley, S. J., & Pearson, A. (2019).
746 Archaeal lipid biomarker constraints on the Paleocene-Eocene carbon isotope excursion.
747 *Nature Communications*, *10*(1), 1–10. https://doi.org/10.1038/s41467-019-12553-3
748 Farrimond, P., Taylor, A., & Telnás, N. (1998). Biomarker maturity parameters : the role of
749 generation and thermal degradation. *Organic Geochemistry*, *29*(5–7), 1181–1197.
750 https://doi.org/10.1016/S0146-6380(98)00079-5
751 French, K. L., Tosca, N. J., Cao, C., & Summons, R. E. (2012). Diagenetic and detrital origin of
752 moretane anomalies through the Permian-Triassic boundary. *Geochimica et Cosmochimica*
753 *Acta*, *84*, 104–125. https://doi.org/10.1016/j.gca.2012.01.004
754 Frieling, J., Svensen, H. H., Planke, S., Cramwinckel, M. J., Selnes, H., & Sluijs, A. (2016).
755 Thermogenic methane release as a cause for the long duration of the PETM. *Proceedings of*
756 *the National Academy of Sciences of the United States of America*, *113*(43), 12059–12064.
757 https://doi.org/10.1073/pnas.1603348113
758 Galy, V., Beyssac, O., France-Lanord, C., & Eglinton, T. (2008). Recycling of Graphite During
759 Himalayan Erosion: A Geological Stabilization of Carbon in the Crust. *Science*, *322*(5903),
760 943–945. https://doi.org/10.1126/science.1161408
761 Galy, V., France-Lanord, C., Beyssac, O., Faure, P., Kudrass, H., & Palhol, F. (2007). Efficient
762 organic carbon burial in the Bengal fan sustained by the Himalayan erosional system.
763 *Nature*, *450*(7168), 407–410. https://doi.org/10.1038/nature06273
764 Galy, V., Peucker-Ehrenbrink, B., & Eglinton, T. (2015). Global carbon export from the
765 terrestrial biosphere controlled by erosion. *Nature*, *521*, 204–207.
766 https://doi.org/10.1038/nature14400
767 Gibson, T. G., Bybell, L. M., & Mason, D. B. (2000). Stratigraphic and climatic implications of
768 clay mineral changes around the Paleocene/Eocene boundary of the northeastern US
769 margin. *Sedimentary Geology*, *134*(1–2), 65–92. https://doi.org/10.1016/S0037-

770 0738(00)00014-2
771 Goñi, M. A., Hatten, J. A., Wheatcroft, R. A., & Borgeld, J. C. (2013). Particulate organic matter
772 export by two contrasting small mountainous rivers from the Pacific Northwest, U.S.A.
773 *Journal of Geophysical Research: Biogeosciences*, *118*(1), 112–134.
774 https://doi.org/10.1002/jgrg.20024
775 Gutjahr, M., Ridgwell, A., Sexton, P. F., Anagnostou, E., Pearson, P. N., Pälike, H., Norris, R.
776 D., Thomas, E., & Foster, G. L. (2017). Very large release of mostly volcanic carbon during
777 the Palaeocene – Eocene Thermal Maximum. *Nature*, *548*, 573–577.
778 https://doi.org/10.1038/nature23646
779 Handley, L., O'Halloran, A., Pearson, P. N., Hawkins, E., Nicholas, C. J., Schouten, S.,
780 McMillan, I. K., & Pancost, R. D. (2012). Changes in the hydrological cycle in tropical East
781 Africa during the Paleocene-Eocene Thermal Maximum. *Palaeogeography,*
782 *Palaeoclimatology, Palaeoecology*, *329–330*, 10–21.
783 https://doi.org/10.1016/j.palaeo.2012.02.002
784 Handley, L., Pearson, P. N., Mcmillan, I. K., & Pancost, R. D. (2008). Large terrestrial and
785 marine carbon and hydrogen isotope excursions in a new Paleocene/Eocene boundary
786 section from Tanzania. *Earth and Planetary Science Letters*, *275*(1), 17–25.
787 https://doi.org/10.1016/j.epsl.2008.07.030
788 Harding, I. C., Charles, A. J., Marshall, J. E. A., Pälike, H., Roberts, A. P., Wilson, P. A., Jarvis,
789 E., Thorne, R., Morris, E., Moremon, R., Pearce, R. B., & Akbari, S. (2011). Sea-level and
790 salinity fluctuations during the Paleocene-Eocene thermal maximum in Arctic Spitsbergen.
791 *Earth and Planetary Science Letters*, *303*(1–2), 97–107.
792 https://doi.org/10.1016/j.epsl.2010.12.043
793 Hilton, R. G. (2017). Climate regulates the erosional carbon export from the terrestrial biosphere.
794 *Geomorphology*, *277*, 118–132. https://doi.org/10.1016/j.geomorph.2016.03.028
795 Hilton, R. G., Gaillardet, J., Calmels, D., & Birck, J. (2014). Geological respiration of a
796 mountain belt revealed by the trace element rhenium. *Earth and Planetary Science Letters*,
797 *403*, 27–36. https://doi.org/10.1016/j.epsl.2014.06.021
798 Hilton, R. G., Galy, A., & Hovius, N. (2008). Riverine particulate organic carbon from an active
799 mountain belt: Importance of landslides. *Global Biogeochemical Cycles*, *22*(1), 1–12.
800 https://doi.org/10.1029/2006GB002905

Hilton, R. G., Galy, A., Hovius, N., Horng, M., & Chen, H. (2011). Efficient transport of fossil organic carbon to the ocean by steep mountain rivers: An orogenic carbon sequestration mechanism. *Geology*, *39*(1), 71–74. https://doi.org/10.1130/G31352.1

Hilton, R. G., Galy, A., Hovius, N., Horng, M. J., & Chen, H. (2010). The isotopic composition of particulate organic carbon in mountain rivers of Taiwan. *Geochimica et Cosmochimica Acta*, *74*(11), 3164–3181. https://doi.org/10.1016/j.gca.2010.03.004

Hilton, R. G., Galy, V., Gaillardet, J., Dellinger, M., Bryant, C., O'Regan, M., Gröcke, D. R., Coxall, H., Bouchez, J., & Calmels, D. (2015). Erosion of organic carbon in the Arctic as a geological carbon dioxide sink. *Nature*, *524*, 84–87. https://doi.org/10.1038/nature14653

Hilton, R. G., & West, A. J. (2020). Mountains, erosion and the carbon cycle. *Nature Reviews Earth & Environment*, *1*, 284–299. https://doi.org/10.1038/s43017-020-0058-6

Hollingsworth, E. H. (2023). Spatial and Temporal Patterns in Petrogenic Organic Carbon Mobilisation during the Paleocene-Eocene Thermal Maximum. [Dataset]. https://doi.org/10.17605/OSF.IO/F8HJC

Inglis, G. N., Bragg, F., Burls, N. J., Cramwinckel, M. J., Evans, D., Foster, G. L., Huber, M., Lunt, D. J., Siler, N., Steinig, S., Tierney, J. E., Wilkinson, R., Anagnostou, E., de Boer, A. M., Dunkley Jones, T., Edgar, K. M., Hollis, C. J., Hutchinson, D. K., & Pancost, R. D. (2020). Global mean surface temperature and climate sensitivity of the early Eocene Climatic Optimum (EECO), Paleocene-Eocene Thermal Maximum (PETM), and latest Paleocene. *Climate of the Past*, *16*(5), 1953–1968. https://doi.org/10.5194/cp-16-1953-2020

Inglis, G. N., Naafs, B. D. A., Zheng, Y., McClymont, E. L., Evershed, R. P., & Pancost, R. D. (2018). Distributions of geohopanoids in peat: Implications for the use of hopanoid-based proxies in natural archives. *Geochimica et Cosmochimica Acta*, *224*, 249–261. https://doi.org/10.1016/j.gca.2017.12.029

John, C. M., Banerjee, N. R., Longstaffe, F. J., Sica, C., Law, K. R., & Zachos, J. C. (2012). Clay assemblage and oxygen isotopic constraints on the weathering response to the Paleocene-Eocene thermal maximum, East Coast of North America. *Geology*, *40*(7), 591–594. https://doi.org/10.1130/G32785.1

John, C. M., Bohaty, S. M., Zachos, J. C., Sluijs, A., Gibbs, S., Brinkhuis, H., & Bralower, T. J. (2008). North American continental margin records of the Paleocene-Eocene thermal maximum: Implications for global carbon and hydrological cycling. *Paleoceanography*,

23(2), 1–20. https://doi.org/10.1029/2007PA001465

Jones, M. T., Percival, L. M. E., Stokke, E. W., Frieling, J., Mather, T. A., Riber, L., Schubert, B. A., Schultz, B., Tegner, C., Planke, S., & Svensen, H. H. (2019). Mercury anomalies across the Palaeocene-Eocene Thermal Maximum. *Climate of the Past*, *15*(1), 217–236. https://doi.org/10.5194/cp-15-217-2019

Kaiho, K., Arinobu, T., Ishiwatari, R., Morgans, H. E. G., Okada, H., Takeda, N., Tazaki, K., Zhou, G., Kajiwara, Y., Matsumoto, R., Hirai, A., Niitsuma, N., & Wada, H. (1996). Latest Paleocene benthic foraminferal extinction and environmental changes at Tawanui , New Zealand. *Paleoceanography*, *11*(4), 447–465. https://doi.org/10.1029/96PA01021

Kao, S. J., Dai, M. H., Wei, K. Y., Blair, N. E., & Lyons, W. B. (2008). Enhanced supply of fossil organic carbon to the Okinawa trough since the last deglaciation. *Paleoceanography*, *23*(2), 1–10. https://doi.org/10.1029/2007PA001440

Kao, S. J., Hilton, R. G., Selvaraj, K., Dai, M., Zehetner, F., Huang, J. C., Hsu, S. C., Sparkes, R., Liu, J. T., Lee, T. Y., Yang, J. Y. T., Galy, A., Xu, X., & Hovius, N. (2014). Preservation of terrestrial organic carbon in marine sediments offshore Taiwan: Mountain building and atmospheric carbon dioxide sequestration. *Earth Surface Dynamics*, *2*(1), 127–139. https://doi.org/10.5194/esurf-2-127-2014

Kaya, M. Y., Dupont-Nivet, G., Frieling, J., Fioroni, C., Rohrmann, A., Altıner, S. Ö., Vardar, E., Tanyaş, H., Mamtimin, M., & Zhaojie, G. (2022). The Eurasian epicontinental sea was an important carbon sink during the Palaeocene-Eocene thermal maximum. *Communications Earth and Environment*, *3*(1), 1–10. https://doi.org/10.1038/s43247-022-00451-4

Kiehl, J. T., Zarzycki, C. M., Shields, C. A., & Rothstein, M. V. (2021). Simulated changes to tropical cyclones across the Paleocene-Eocene Thermal Maximum (PETM) boundary. *Palaeogeography, Palaeoclimatology, Palaeoecology*, *572*, 110421. https://doi.org/10.1016/j.palaeo.2021.110421

Kirtland Turner, S. (2018). Constraints on the onset duration of the Paleocene-Eocene Thermal Maximum. *Philosophical Transactions of the Royal Society A*, *376*(2130), 1–16. https://doi.org/10.1098/rsta.2017.0082

Kopp, R. E., Schumann, D., Raub, T. D., Powars, D. S., Godfrey, L. V., Swanson-Hysell, N. L., Maloof, A. C., & Vali, H. (2009). An Appalachian Amazon? Magnetofossil evidence for the

development of a tropical river-like system in the mid-Atlantic United States during the Paleocene-Eocene thermal maximum. *Paleoceanography*, *24*(4), 1–17. https://doi.org/10.1029/2009PA001783

Korasidis, V. A., Wing, S. L., Shields, C. A., & Kiehl, J. T. (2022). Global Changes in Terrestrial Vegetation and Continental Climate During the Paleocene-Eocene Thermal Maximum. *Paleoceanography and Paleoclimatology*, *37*(4), 1–21. https://doi.org/10.1029/2021PA004325

Kraus, M. J., McInerney, F. A., Wing, S. L., Secord, R., Baczynski, A. A., & Bloch, J. I. (2013). Paleohydrologic response to continental warming during the Paleocene-Eocene Thermal Maximum, Bighorn Basin, Wyoming. *Palaeogeography, Palaeoclimatology, Palaeoecology*, *370*, 196–208. https://doi.org/10.1016/j.palaeo.2012.12.008

Kraus, M. J., & Riggins, S. (2007). Transient drying during the Paleocene-Eocene Thermal Maximum (PETM): Analysis of paleosols in the bighorn basin, Wyoming. *Palaeogeography, Palaeoclimatology, Palaeoecology*, *245*(3–4), 444–461. https://doi.org/10.1016/j.palaeo.2006.09.011

Kurtz, A. C., Kump, L. R., Arthur, M. A., Zachos, J. C., & Paytan, A. (2003). Early Cenozoic decoupling of the global carbon and sulfur cycles. *Paleoceanography*, *18*(4), 1–14. https://doi.org/10.1029/2003PA000908

Kusch, S., & Rush, D. (2022). Revisiting the precursors of the most abundant natural products on Earth: A look back at 30+ years of bacteriohopanepolyol (BHP) research and ahead to new frontiers. *Organic Geochemistry*, *172*, 104469. https://doi.org/10.1016/j.orggeochem.2022.104469

Lee, J.-Y., Marotzke, J., Bala, G., Cao, L., Corti, S., Dunne, J. P., Engelbrecht, F., Fischer, E., Fyfe, J. C., Jones, C., Maycock, A., Mutemi, J., Ndiaye, O., Panickal, S., & Zhou, T. (2021). Future Global Climate: Scenario-based Projections and Near-term Information Coordinating. In and B. Z. Masson-Delmotte, V., P. Zhai, A. Pirani, S.L. Connors, C. Péan, S. Berger, N. Caud, Y. Chen, L. Goldfarb, M.I. Gomis, M. Huang, K. Leitzell, E. Lonnoy, J.B.R. Matthews, T.K. Maycock, T. Waterfield, O. Yelekçi, R. Yu (Ed.), *Climate Change 2021: The Physical Science Basis. Contribution of Working Group I to the Sixth Assessment Report of the Intergovernmental Panel on Climate Change*. Cambridge University Press. https://doi.org/10.1017/9781009157896.006.553

Leithold, E. L., Blair, N. E., & Perkey, D. W. (2006). Geomorphologic controls on the age of particulate organic carbon from small mountainous and upland rivers. *Global Biogeochemical Cycles*, *20*(3), 1–11. https://doi.org/10.1029/2005GB002677

Lyons, S. L., Baczynski, A. A., Babila, T. L., Bralower, T. J., Hajek, E. A., Kump, L. R., Polites, E. G., Self-Trail, J. M., Trampush, S. M., Vornlocher, J. R., Zachos, J. C., & Freeman, K. H. (2019). Palaeocene–Eocene Thermal Maximum prolonged by fossil carbon oxidation. *Nature Geoscience*, *12*, 54–60. https://doi.org/10.1038/s41561-018-0277-3

Lyster, S. J., Whittaker, A. C., Allison, P. A., Lunt, D. J., & Farnsworth, A. (2020). Predicting sediment discharges and erosion rates in deep time—examples from the late Cretaceous North American continent. *Basin Research*, *32*(6), 1547–1573. https://doi.org/10.1111/bre.12442

Mackenzie, A. S., Patience, R. L., Maxwell, J. R., Vandenbroucke, M., & Durand, B. (1980). Molecular parameters of maturation in the Toarcian shales, Paris Basin, France—I. Changes in the configurations of acyclic isoprenoid alkanes, steranes and triterpanes. *Geochimica et Cosmochimica Acta*, *44*(11), 1709–1721. https://doi.org/10.1016/0016-7037(80)90222-7

McInerney, F. A., & Wing, S. L. (2011). The Paleocene-Eocene Thermal Maximum: A perturbation of carbon cycle, climate, and biosphere with implications for the future. *Annual Review of Earth and Planetary Sciences*, *39*, 489–516. https://doi.org/10.1146/annurev-earth-040610-133431

Meyers, S. R. (2014). *Astrochron: An R Package for Astrochronology https://cran.r-project.org/package=astrochron*.

Murphy, B. H., Farley, K. A., & Zachos, J. C. (2010). An extraterrestrial 3He-based timescale for the Paleocene-Eocene thermal maximum (PETM) from Walvis Ridge, IODP Site 1266. *Geochimica et Cosmochimica Acta*, *74*(17), 5098–5108. https://doi.org/10.1016/j.gca.2010.03.039

Pagani, M., Pedentchouk, N., Huber, M., Sluijs, A., Schouten, S., Brinkhuis, H., Dickens, G. R., Sinninghe Damsté, J. S., & Scientists, E. 302. (2006). Arctic hydrology during global warming at the Palaeocene / Eocene thermal maximum. *Nature*, *442*(7103), 671–675. https://doi.org/10.1038/nature05043

Pancost, R. D., Coleman, J. M., Love, G. D., Chatzi, A., Bouloubassi, I., & Snape, C. E. (2008). Kerogen-bound glycerol dialkyl tetraether lipids released by hydropyrolysis of marine

925 sediments: A bias against incorporation of sedimentary organisms? *Organic Geochemistry*,
926 *39*(9), 1359–1371. https://doi.org/10.1016/j.orggeochem.2008.05.002
927 Papadomanolaki, N. M., Sluijs, A., & Slomp, C. P. (2022). Eutrophication and Deoxygenation
928 Forcing of Marginal Marine Organic Carbon Burial During the PETM. *Paleoceanography*
929 *and Paleoclimatology*, *37*(3), 1–23. https://doi.org/10.1029/2021PA004232
930 Peters, K. E., Walters, C. C., & Moldowan, J. M. (2005). *The Biomarker Guide Vols 1*.
931 Cambridge University Press.
932 Petsch, S. T., Berner, R. A., & Eglinton, T. I. (2000). A field study of the chemical weathering of
933 ancient sedimentary organic matter. *Organic Geochemistry*, *31*(5), 475–487.
934 https://doi.org/10.1016/S0146-6380(00)00014-0
935 Polik, C. A., Elling, F. J., & Pearson, A. (2018). Impacts of Paleoecology on the TEX 86 Sea
936 Surface Temperature Proxy in the Pliocene-Pleistocene Mediterranean Sea.
937 *Paleoceanography and Paleoclimatology*, *33*(12), 1472–1489.
938 https://doi.org/10.1029/2018PA003494
939 Robert, C., & Kennett, J. P. (1994). Antarctic subtropical humid episode at the Paleocene-Eocene
940 boundary: clay-mineral evidence. *Geology*, *22*(3), 211–214. https://doi.org/10.1130/0091-
941 7613(1994)022<0211:ASHEAT>2.3.CO;2
942 Röhl, U., Westerhold, T., Bralower, T. J., & Zachos, J. C. (2007). On the duration of the
943 Paleocene-Eocene thermal maximum (PETM). *Geochemistry, Geophysics, Geosystems*,
944 *8*(12), 1–13. https://doi.org/10.1029/2007GC001784
945 Rosa-Putra, S., Nalin, R., Domenach, A. M., & Rohmer, M. (2001). Novel hopanoids from
946 Frankia spp. and related soil bacteria: Squalene cyclization and significance of geological
947 biomarkers revisited. *European Journal of Biochemistry*, *268*(15), 4300–4306.
948 https://doi.org/10.1046/j.1432-1327.2001.02348.x
949 Rush, W. D., Kiehl, J. T., Shields, C. A., & Zachos, J. C. (2021). Increased frequency of extreme
950 precipitation events in the North Atlantic during the PETM: Observations and theory.
951 *Palaeogeography, Palaeoclimatology, Palaeoecology*, *568*, 110289.
952 https://doi.org/10.1016/j.palaeo.2021.110289
953 Schmitz, B., & Pujalte, V. (2003). Sea-level , humidity , and land-erosion records across the
954 initial Eocene thermal maximum from a continental-marine transect in northern Spain.
955 *Geology*, *31*(8), 689–692. https://doi.org/10.1130/G19527.1

Schmitz, B., & Pujalte, V. (2007). Abrupt increase in seasonal extreme precipitation at the Paleocene-Eocene boundary. *Geology*, *35*(3), 215–218. https://doi.org/10.1130/G23261A.1

Self-Trail, J. M., Robinson, M. M., Bralower, T. J., Sessa, J. A., Hajek, E. A., Kump, L. R., Trampush, S. M., Willard, D. A., Edwards, L. E., Powars, D. S., & Wandless, G. A. (2017). Shallow marine response to global climate change during the Paleocene-Eocene Thermal Maximum, Salisbury Embayment, USA. *Paleoceanography*, *32*(7), 710–728. https://doi.org/10.1002/2017PA003096

Shcherbinina, E., Gavrilov, Y., Iakovleva, A., Pokrovsky, B., Golovanova, O., & Aleksandrova, G. (2016). Environmental dynamics during the Paleocene-Eocene thermal maximum (PETM) in the northeastern Peri-Tethys revealed by high-resolution micropalaeontological and geochemical studies of a Caucasian key section. *Palaeogeography, Palaeoclimatology, Palaeoecology*, *456*, 60–81. https://doi.org/10.1016/j.palaeo.2016.05.006

Shields, C. A., Kiehl, J. T., Rush, W., Rothstein, M., & Snyder, M. A. (2021). Atmospheric rivers in high-resolution simulations of the Paleocene Eocene Thermal Maximum (PETM). *Palaeogeography, Palaeoclimatology, Palaeoecology*, *567*, 110293. https://doi.org/10.1016/j.palaeo.2021.110293

Sluijs, A., Bijl, P. K., Schouten, S., Röhl, U., Reichart, G.-J., & Brinkhuis, H. (2011). Southern ocean warming , sea level and hydrological change during the Paleocene-Eocene thermal maximum. *Climate of the Past*, *7*(1), 47–61. https://doi.org/10.5194/cp-7-47-2011

Sluijs, A., & Brinkhuis, H. (2009). A dynamic climate and ecosystem state during the Paleocene-Eocene Thermal Maximum: Inferences from dinoflagellate cyst assemblages on the New Jersey Shelf. *Biogeosciences*, *6*(8), 1755–1781. https://doi.org/10.5194/bg-6-1755-2009

Sluijs, A., Brinkhuis, H., Crouch, E. M., John, C. M., Handley, L., Munsterman, D., Bohaty, S. M., Zachos, J. C., Reichart, G. J., Schouten, S., Pancost, R. D., Damsté, J. S. S., Welters, N. L. D., Lotter, A. F., & Dickens, G. R. (2008). Eustatic variations during the Paleocene-Eocene greenhouse world. *Paleoceanography*, *23*(4), 1–18. https://doi.org/10.1029/2008PA001615

Sluijs, A., Frieling, J., Inglis, G. N., Nierop, K. G. J., Peterse, F., Sangiorgi, F., & Schouten, S. (2020). Late Paleocene–early Eocene Arctic Ocean sea surface temperatures: reassessing biomarker paleothermometry at Lomonosov Ridge. *Climate of the Past*, *16*(6), 2381–2400. https://doi.org/10.5194/cp-16-2381-2020

Sluijs, A., Röhl, U., Schouten, S., Brumsack, H.-I., Sangiorgi, F., Sinninghe Damsté, J. S., & Brinkhuis, H. (2008). Arctic late Paleocene–early Eocene paleoenvironments with special emphasis on the Paleocene-Eocene thermal maximum (Lomonosov Ridge , Integrated Ocean Drilling Program Expedition 302). *Paleoceanography*, *23*(1), 1–17. https://doi.org/10.1029/2007PA001495

Sluijs, A., Schouten, S., Pagani, M., Woltering, M., Brinkhuis, H., Dickens, G. R., Huber, M., Reichart, G., Stein, R., Matthiessen, J., Lourens, L. J., Pedentchouk, N., Backman, J., & Moran, K. (2006). Subtropical Arctic Ocean temperatures during the Palaeocene/Eocene thermal maximum. *Nature*, *441*(1), 610–613. https://doi.org/10.1038/nature04668

Sluijs, A., van Roij, L., Harrington, G. J., Schouten, S., Sessa, J. A., Levay, L. J., Reichart, G.-J., & Slomp, C. P. (2014). Warming , euxinia and sea level rise during the Paleocene-Eocene Thermal Maximum on the Gulf Coastal Plain: implications for ocean oxygenation and nutrient cycling. *Climate of the Past*, *10*(4), 1421–1439. https://doi.org/10.5194/cp-10-1421-2014

Smith, J. C., Galy, A., Hovius, N., Tye, A. M., Turowski, J. M., & Schleppi, P. (2013). Runoff-driven export of particulate organic carbon from soil in temperate forested uplands. *Earth and Planetary Science Letters*, *365*, 198–208. https://doi.org/10.1016/j.epsl.2013.01.027

Stallard, R. F. (1998). Terrestrial sedimentation and the carbon cycle: Coupling weathering and erosion to carbon burial. *Global Biogeochemical Cycles*, *12*(2), 231–257. https://doi.org/10.1029/98GB00741

Stassen, P., Thomas, E., & Speijer, R. P. (2012). Integrated stratigraphy of the Paleocene-Eocene thermal maximum in the New Jersey Coastal Plain: Toward understanding the effects of global warming in a shelf environment. *Paleoceanography*, *27*(4), 1–17. https://doi.org/10.1029/2012PA002323

Storey, M., Duncan, R. A., & Swisher, C. C. (2007). Paleocene-Eocene thermal maximum and the opening of the northeast Atlantic. *Science*, *316*(5824), 587–589. https://doi.org/10.1126/science.1135274

Svensen, H., Planke, S., Maithe-Sørensen, A., Jamtveit, B., Myklebust, R., Eidem, T. R., & Rey, S. S. (2004). Release of methane from a volcanic basin as a mechanism for initial Eocene global warming. *Nature*, *429*, 542–545. https://doi.org/10.1038/nature02566

Tierney, J. E., Zhu, J., Li, M., Ridgwell, A., Hakim, G. J., Poulsen, C. J., Whiteford, R. D. M.,

Rae, J. W. B., & Kump, L. R. (2022). Spatial patterns of climate change across the Paleocene–Eocene Thermal Maximum. *Proceedings of the National Academy of Sciences of the United States of America*, *119*(42), 1–7. https://doi.org/10.1073/pnas.2205326119

Walker, J. C. G., Hays, P. B., & Kasting, J. F. (1981). A Negative Feedback Mechanism for the Long-term Stabilization of Earth's Surface Temperature. *Journal of Geophysical Research*, *86*(10), 9776–9782. https://doi.org/10.1029/JC086iC10p09776

Winguth, A., Shellito, C., Shields, C., & Winguth, C. (2010). Climate response at the paleocene-eocene thermal maximum to greenhouse gas forcing-a model study with CCSM3. *Journal of Climate*, *23*(10), 2562–2584. https://doi.org/10.1175/2009JCLI3113.1

Zeebe, R. E. (2013). What caused the long duration of the Paleocene-Eocene Thermal Maximum. *Paleoceanography*, *28*(3), 440–452. https://doi.org/10.1002/palo.20039

Zeebe, R. E., Dickens, G. R., Ridgwell, A., Sluijs, A., & Thomas, E. (2014). Onset of carbon isotope excursion at the Paleocene-Eocene thermal maximum took millennia, not 13 years. *Proceedings of the National Academy of Sciences of the United States of America*, *111*(12), 1062–1063. https://doi.org/10.1073/pnas.1321177111

Zeebe, R. E., & Lourens, L. J. (2019). Solar System chaos and the Paleocene–Eocene boundary age constrained by geology and astronomy. *Science*, *929*(6456), 926–929. https://doi.org/10.1126/science.aax0612

Zeebe, R. E., Zachos, J. C., & Dickens, G. R. (2009). Carbon dioxide forcing alone insufficient to explain Palaeocene-Eocene Thermal Maximum warming. *Nature Geoscience*, *2*, 576–580. https://doi.org/10.1038/ngeo578

References from the Supporting Information

Aze, T., Pearson, P. N., Dickson, A. J., Badger, M. P. S., Bown, P. R., Pancost, R. D., Gibbs, S. J., Huber, B. T., Leng, M. J., Coe, A. L., Cohen, A. S., & Foster, G. L. (2014). Extreme warming of tropical waters during the Paleocene – Eocene Thermal Maximum. *Geology*, *42*(9), 739–742. https://doi.org/10.1130/G35637.1

Bolle, M. P., Pardo, A., Hinrichs, K. U., Adatte, T., Von Salis, K., Burns, S., Keller, G., & Muzylev, N. (2000). The Paleocene-Eocene transition in the marginal northeastern Tethys (Kazakhstan and Uzbekistan). *International Journal of Earth Sciences*, *89*(2), 390–414. https://doi.org/10.1007/s005310000092

Bralower, T. J., Kump, L. R., Self-Trail, J. M., Robinson, M. M., Lyons, S., Babila, T., Ballaron, E., Freeman, K. H., Hajek, E., Rush, W., & Zachos, J. C. (2018). Evidence for Shelf Acidification During the Onset of the Paleocene-Eocene Thermal Maximum. *Paleoceanography and Paleoclimatology*, *33*(12), 1408–1426. https://doi.org/10.1029/2018PA003382

Dickson, A. J., Rees-owen, R. L., März, C., Coe, A. L., Cohen, A. S., Pancost, R. D., Taylor, K., & Shcherbinina, E. (2014). The spread of marine anoxia on the northern Tethys margin during the Paleocene-Eocene Thermal Maximum. *Paleoceanography*, *29*(6), 471–488. https://doi.org/10.1002/2014PA002629.Received

Doubrawa, M., Stassen, P., Robinson, M. M., Babila, T. L., Zachos, J. C., & Speijer, R. P. (2022). Shelf Ecosystems Along the U.S. Atlantic Coastal Plain Prior to and During the Paleocene-Eocene Thermal Maximum: Insights Into the Stratigraphic Architecture. *Paleoceanography and Paleoclimatology*, *37*(10), 1–21. https://doi.org/10.1029/2022PA004475

Elling, F. J., Gottschalk, J., Doeana, K. D., Kusch, S., Hurley, S. J., & Pearson, A. (2019). Archaeal lipid biomarker constraints on the Paleocene-Eocene carbon isotope excursion. *Nature Communications*, *10*(1), 1–10. https://doi.org/10.1038/s41467-019-12553-3

Gavrilov, Y. O., Shcherbinina, E. A., & Oberhänsli, H. (2003). Paleocene-Eocene boundary events in the northeastern Peri-Tethys. *Special Paper of the Geological Society of America*, *369*, 147–168. https://doi.org/10.1130/0-8137-2369-8.147

Handley, L., O'Halloran, A., Pearson, P. N., Hawkins, E., Nicholas, C. J., Schouten, S., McMillan, I. K., & Pancost, R. D. (2012). Changes in the hydrological cycle in tropical East Africa during the Paleocene-Eocene Thermal Maximum. *Palaeogeography, Palaeoclimatology, Palaeoecology*, *329–330*, 10–21. https://doi.org/10.1016/j.palaeo.2012.02.002

Handley, L., Pearson, P. N., Mcmillan, I. K., & Pancost, R. D. (2008). Large terrestrial and marine carbon and hydrogen isotope excursions in a new Paleocene/Eocene boundary section from Tanzania. *Earth and Planetary Science Letters*, *275*(1), 17–25. https://doi.org/10.1016/j.epsl.2008.07.030

Harris, A. D., Miller, K. G., Browning, J. V., Sugarman, P. J., Olsson, R. K., Cramer, B. S., & Wright, J. D. (2010). Integrated stratigraphic studies of Paleocene-lowermost Eocene

sequences, New Jersey Coastal Plain: Evidence for glacioeustatic control. *Paleoceanography*, *25*(3), 1–18. https://doi.org/10.1029/2009PA001800

Hollis, C. J., Dunkley Jones, T., Anagnostou, E., Bijl, P. K., Cramwinckel, M. J., Cui, Y., Dickens, G. R., Edgar, K. M., Eley, Y., Evans, D., Foster, G. L., Frieling, J., Inglis, G. N., Kennedy, E. M., Kozdon, R., Lauretano, V., Lear, C. H., Littler, K., Lourens, L., … Lunt, D. J. (2019). The DeepMIP contribution to PMIP4: Methodologies for selection, compilation and analysis of latest Paleocene and early Eocene climate proxy data, incorporating version 0.1 of the DeepMIP database. *Geoscientific Model Development*, *12*(7), 3149–3206. https://doi.org/10.5194/gmd-12-3149-2019

John, C. M., Bohaty, S. M., Zachos, J. C., Sluijs, A., Gibbs, S., Brinkhuis, H., & Bralower, T. J. (2008). North American continental margin records of the Paleocene-Eocene thermal maximum: Implications for global carbon and hydrological cycling. *Paleoceanography*, *23*(2), 1–20. https://doi.org/10.1029/2007PA001465

Junium, C. K., Dickson, A. J., & Uveges, B. T. (2018). Perturbation to the nitrogen cycle during rapid Early Eocene global warming. *Nature Communications*, *9*(1). https://doi.org/10.1038/s41467-018-05486-w

Lyons, S. L., Baczynski, A. A., Babila, T. L., Bralower, T. J., Hajek, E. A., Kump, L. R., Polites, E. G., Self-Trail, J. M., Trampush, S. M., Vornlocher, J. R., Zachos, J. C., & Freeman, K. H. (2019). Palaeocene–Eocene Thermal Maximum prolonged by fossil carbon oxidation. *Nature Geoscience*, *12*, 54–60. https://doi.org/10.1038/s41561-018-0277-3

Self-Trail, J. M., Powars, D. S., Watkins, D. K., & Wandless, G. A. (2012). Calcareous nannofossil assemblage changes across the Paleocene-Eocene Thermal Maximum: Evidence from a shelf setting. *Marine Micropaleontology*, *92–93*, 61–80. https://doi.org/10.1016/j.marmicro.2012.05.003

Shcherbinina, E., Gavrilov, Y., Iakovleva, A., Pokrovsky, B., Golovanova, O., & Aleksandrova, G. (2016). Environmental dynamics during the Paleocene-Eocene thermal maximum (PETM) in the northeastern Peri-Tethys revealed by high-resolution micropalaeontological and geochemical studies of a Caucasian key section. *Palaeogeography, Palaeoclimatology, Palaeoecology*, *456*, 60–81. https://doi.org/10.1016/j.palaeo.2016.05.006

Sluijs, A., Bijl, P. K., Schouten, S., Röhl, U., Reichart, G.-J., & Brinkhuis, H. (2011). Southern ocean warming , sea level and hydrological change during the Paleocene-Eocene thermal

maximum. *Climate of the Past*, *7*(1), 47–61. https://doi.org/10.5194/cp-7-47-2011

Sluijs, A., Röhl, U., Schouten, S., Brumsack, H.-I., Sangiorgi, F., Sinninghe Damsté, J. S., & Brinkhuis, H. (2008). Arctic late Paleocene–early Eocene paleoenvironments with special emphasis on the Paleocene-Eocene thermal maximum (Lomonosov Ridge , Integrated Ocean Drilling Program Expedition 302). *Paleoceanography*, *23*(1), 1–17. https://doi.org/10.1029/2007PA001495

Sluijs, A., Schouten, S., Pagani, M., Woltering, M., Brinkhuis, H., Dickens, G. R., Huber, M., Reichart, G., Stein, R., Matthiessen, J., Lourens, L. J., Pedentchouk, N., Backman, J., & Moran, K. (2006). Subtropical Arctic Ocean temperatures during the Palaeocene/Eocene thermal maximum. *Nature*, *441*(1), 610–613. https://doi.org/10.1038/nature04668

Stassen, P., Thomas, E., & Speijer, R. P. (2012). Integrated stratigraphy of the Paleocene-Eocene thermal maximum in the New Jersey Coastal Plain: Toward understanding the effects of global warming in a shelf environment. *Paleoceanography*, *27*(4), 1–17. https://doi.org/10.1029/2012PA002323